LETTER

doi:10.1038/nature17965

Neural correlates of single-vessel haemodynamic responses *in vivo*

Philip O'Herron[1], Pratik Y. Chhatbar[1], Manuel Levy[1], Zhiming Shen[1], Adrien E. Schramm[1], Zhongyang Lu[1] & Prakash Kara[1]

Neural activation increases blood flow locally. This vascular signal is used by functional imaging techniques to infer the location and strength of neural activity[1,2]. However, the precise spatial scale over which neural and vascular signals are correlated is unknown. Furthermore, the relative role of synaptic and spiking activity in driving haemodynamic signals is controversial[3–9]. Previous studies recorded local field potentials as a measure of synaptic activity together with spiking activity and low-resolution haemodynamic imaging. Here we used two-photon microscopy to measure sensory-evoked responses of individual blood vessels (dilation, blood velocity) while imaging synaptic and spiking activity in the surrounding tissue using fluorescent glutamate and calcium sensors. In cat primary visual cortex, where neurons are clustered by their preference for stimulus orientation, we discovered new maps for excitatory synaptic activity, which were organized similarly to those for spiking activity but were less selective for stimulus orientation and direction. We generated tuning curves for individual vessel responses for the first time and found that parenchymal vessels in cortical layer 2/3 were orientation selective. Neighbouring penetrating arterioles had different orientation preferences. Pial surface arteries in cats, as well as surface arteries and penetrating arterioles in rat visual cortex (where orientation maps do not exist[10]), responded to visual stimuli but had no orientation selectivity. We integrated synaptic or spiking responses around individual parenchymal vessels in cats and established that the vascular and neural responses had the same orientation preference. However, synaptic and spiking responses were more selective than vascular responses—vessels frequently responded robustly to stimuli that evoked little to no neural activity in the surrounding tissue. Thus, local neural and haemodynamic signals were partly decoupled. Together, these results indicate that intrinsic cortical properties, such as propagation of vascular dilation between neighbouring columns, need to be accounted for when decoding haemodynamic signals.

To determine how neural activity leads to changes in cerebral blood flow, the haemodynamic responses of individual vessels need to be compared to neural activity in the surrounding tissue[11]. While sensory-evoked responses of individual vessels have been measured in the somatosensory cortex and olfactory bulb of rodents, these studies have not measured vessel responses to the full range of stimuli for which the neighbouring neural tissue is responsive. Thus, the degree to which vascular signals match local neural activity has been difficult to assess. Here we compare neural and vascular responses to a full range of stimulus orientations in cat primary visual cortex to determine if vascular responses can be predicted from local neural activity. Additionally, the primary visual cortex of the cat, similar to that of primates including humans, is organized into precise maps such that different columns of neural tissue are optimally activated by different stimulus orientations (Fig. 1a). Therefore the orientation selectivity of vessel responses can be linked to the spatial scale of neurovascular coupling. For example, if blood flow in a single cortical vessel is sensitive to neural activity over a large spatial scale covering many orientation columns, then the vessel should dilate to a broad range of stimulus orientations. By contrast, if the vascular response is controlled very locally, that is, within the scale of an orientation column, then individual vessels may be highly orientation selective.

We first labelled blood vessels in the cat primary visual cortex with the fluorescent indicators Texas Red Dextran or Alexa 633 (see Methods)[12], and measured the dilation responses to drifting grating stimuli of different orientations. Veins and capillaries, which were distinguished from arteries by a number of means[12] (see Methods), were not included in this initial analysis because they rarely exhibit rapid sensory-evoked dilation[12–14]. Our data set included all other blood vessels, provided that they were sufficiently labelled and imaged in tissue with minimal movements from respiration. All blood vessels in this data set dilated in response to drifting grating visual stimuli ($P < 0.05$ analysis of variance (ANOVA)). Specifically, we found that parenchymal arterioles in layer 2/3 typically dilated more strongly in response to one or two of the stimulus orientations presented (Fig. 1b), whereas pial surface arteries dilated to all orientations nearly equally (Fig. 1c). For each vessel, we computed the orientation selectivity index (OSI; see Methods), such that when a vessel dilates equally to all stimulus orientations the OSI = 0 and when a vessel responds only to a single orientation the OSI = 1. The OSI was much greater for parenchymal arterioles than for pial surface arteries (OSI parenchymal arteriole mean ± standard error of the mean (s.e.m.) = 0.21 ± 0.01; $n = 79$ vessels and OSI surface artery mean ± s.e.m. = 0.06 ± 0.01; $n = 24$ vessels; $P < 10^{-10}$; Mann–Whitney test; Fig. 1d).

To illustrate further the role of an organized map of neocortical neurons in generating tuned parenchymal vessel responses, we also measured dilation changes in rat primary visual cortex. Because cortical neurons in rats are not organized in an orientation map[10], each parenchymal vessel is surrounded by neurons displaying a variety of orientation preferences (Fig. 1e). In rats, we found no orientation selectivity in cortical layer 2/3 parenchymal arterioles (Fig. 1f; OSI mean ± s.e.m. = 0.06 ± 0.01; $n = 16$ vessels) or pial surface arteries (Fig. 1g; OSI mean ± s.e.m. = 0.05 ± 0.01; $n = 21$ vessels) (Fig. 1h).

To compare the orientation selectivity of cat parenchymal vessels to spiking activity in the surrounding tissue, we performed calcium imaging using Oregon Green BAPTA-1 AM (OGB-1 AM) or GCaMP6s, along with vascular imaging from the same sites (see Methods). Figure 2a shows a penetrating arteriole that dilates most strongly to the same stimulus orientation as preferred by the immediately adjacent cortical neurons. However, the vessel also dilated when other stimulus orientations were presented, despite minimal or non-existent responses in the nearby neurons. As a result, the vessel had a substantially broader OSI (0.20) than the neuronal spiking activity (OSI = 0.82, average across six adjacent neurons labelled in Fig. 2a). As a penetrating arteriole is likely to be sensitive to neural activity from more than just the immediately adjacent cells, we examined whether spiking activity over

[1]Department of Neuroscience, Medical University of South Carolina, Charleston, South Carolina 29425, USA.

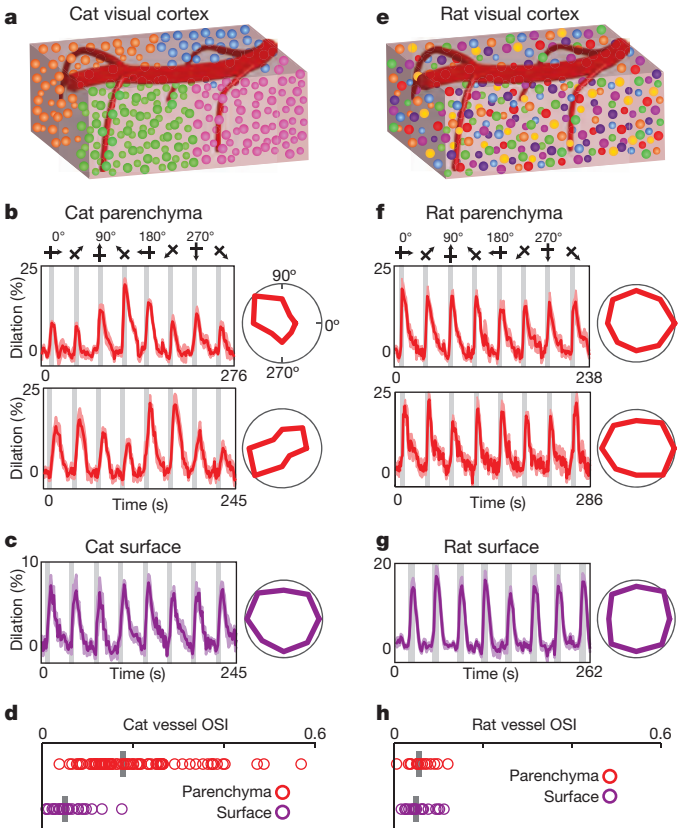

Figure 1 | Selectivity of blood vessel dilation to sensory stimuli in species with and without cortical orientation maps. a, Schematic of cat visual cortex showing the columnar organization of neurons by orientation preference and a pial surface artery with multiple branches penetrating the parenchyma. Different colours of neuronal cell bodies represent their different preferred stimulus orientations. **b**, Time courses and polar plots (averages of six (top) and eight (bottom) trials) of the changes in dilation of two layer 2/3 arterioles in cat visual cortex to visual stimulation. Error bands represent s.e.m. and grey bars represent the periods of visual stimulation. In this and subsequent figures, stimuli were gratings that drifted in eight different directions of motion and polar plots are normalized to the maximum response. **c**, Time course and polar plot of responses from a surface artery in cat (average of four trials). **d**, Population distribution and median OSI for parenchymal ($n = 79$ vessels in 18 cats) and surface ($n = 24$ vessels in 9 cats) vessels. **e**, Schematic of rat visual cortex where neurons with different orientation preferences are intermingled. **f**, **g**, Time courses and polar plots of responses from two parenchymal arterioles (averages of seven (top) and eight (bottom) trials) and a surface artery (average of five trials) in rat visual cortex. **h**, Population distribution and median OSI for parenchymal ($n = 16$ vessels in 6 rats) and surface ($n = 21$ vessels in 7 rats) vessels.

a larger region might explain the broad orientation selectivity of the parenchymal vessels. Previous work has shown that occlusion of a single penetrating arteriole in the neocortex leads to tissue death in regions with approximately 400 μm diameter[15], suggesting that this is the region of tissue that an individual penetrating arteriole supplies (see also Supplementary Information). Therefore we compared vascular responses to calcium signals integrated over 400-μm-diameter windows around each parenchymal artery (Fig. 2b, c). The orientation preference of these regions of spiking activity matched those of the arteries at their centres (Fig. 2d; $R = 0.94$, $n = 19$ pairs, $P < 10^{-8}$). However, the orientation selectivity of the spiking activity was higher than the corresponding artery in all regions examined (Fig. 2e; $P < 10^{-9}$, paired t-test). Because the spacing of penetrating arterioles is heterogeneous (see Supplementary Information), we also examined the selectivity of neural responses in a wide range of window sizes around each vessel (100–600 μm diameter). We found that for all window sizes the spiking activity OSI was still at least 60% higher than the vessel dilation OSI (Fig. 2f; $P < 10^{-5}$ at each window size).

Our calcium imaging results suggest that additional sources of neural activity (besides spiking in the local tissue around the vessel) may be contributing to sensory-evoked vasodilation. Experimental and theoretical work has implicated synaptic glutamate release as a driver of haemodynamic responses[16]. In particular, calculation of the energy budget of the neocortex estimated that, of all the cellular processes performed, excitatory synaptic activity has the largest metabolic demand[17]. Therefore, to measure directly excitatory synaptic activity over different spatial scales and compare it to single-vessel responses, we labelled neurons in the cat visual cortex with a glutamate sensor (iGluSnFR; see Methods). We found that glutamate activity (like neuronal spiking) is organized in direction and orientation maps (Fig. 3 and Extended Data Fig. 1). However, glutamate signals were generally less orientation selective than spiking activity. Integrating over 400-μm-diameter windows, the OSI for calcium (mean ± s.e.m. = 0.59 ± 0.02; $n = 19$ regions) was sharper than that for glutamate (mean ± s.e.m. = 0.44 ± 0.02; $n = 37$ regions; $P < 0.001$, Mann–Whitney test). To determine if excitatory synaptic activity alone could account for single-vessel haemodynamic responses, we integrated the glutamate signals over 400-μm-diameter regions around individual arteries (Fig. 3a, b) and compared these to vessel responses from the same sites (Fig. 3b–e). We found that the visual stimulus that produced the largest glutamate signal in a 400 μm window matched the visual stimulus that resulted in the largest vessel dilation (Fig. 3c; $R = 0.90$, $n = 37$ pairs, $P < 10^{-13}$). However, a 400-μm region of synaptic activity was always more selective than its corresponding penetrating arteriole (Fig. 3d; $P < 10^{-11}$, paired t-test). The mismatch between orientation selectivity in individual blood vessels and synaptic activity was confirmed for a range of glutamate response window sizes (100–600 μm diameter; Fig. 3e; $P < 10^{-5}$ at each window size).

The broader tuning of the vascular response relative to synaptic and spiking activity (Figs 2 and 3) suggests that vessels can respond to sensory stimuli that evoke little to no concomitant neural activity in the surrounding tissue. This phenomenon can be directly observed by comparing the response amplitudes of vessel dilation and neural activity to individual stimulus conditions. Extended Data Figure 2a, b shows an example in which two visual stimuli (135° and 180°) evoked robust dilations in a penetrating arteriole but essentially no glutamate release in the region around the blood vessel. Across the data sets of synaptic and spiking activity, we compared the amplitude of each vessel's response to each sensory stimulus against the neural response around the vessel to the same stimulus (Extended Data Fig. 2c). Our analysis confirmed that there are many instances where there is a non-existent (or very small) synaptic or spiking response to a visual stimulus despite a robust dilation response. In general, there are very few instances where a stimulus failed to evoke a dilation response of some magnitude.

Like orientation tuning, direction selectivity is a hallmark feature of the primary visual cortex and represents the capacity of a neuron to respond preferentially to one direction of stimulus motion at the optimal stimulus orientation. We found direction maps for excitatory synaptic activity (Fig. 3) that were qualitatively similar to direction maps of spiking activity (Fig. 2). However, the directionality index[10] (DI) over 400-μm-diameter windows was greater for spiking activity than for synaptic responses (DI spiking mean ± s.e.m. = 0.59 ± 0.07; $n = 19$ regions; DI synaptic mean ± s.e.m. = 0.33 ± 0.03; $n = 37$ regions; $P < 0.01$; Extended Data Fig. 3a). Blood vessel responses appeared to have little direction selectivity, even when surrounded by iso-direction territories of spiking activity, for example, Fig. 2b vessels 2 and 4. Indeed, across the population, the direction selectivity of vessels was smaller than that of regions of spiking activity (DI vessel mean ± s.e.m. = 0.30 ± 0.02; $n = 79$ vessels; $P < 0.0005$). The population mean DI of vessels and synaptic activity were similar (Extended Data Fig. 3a; $P = 0.70$) although

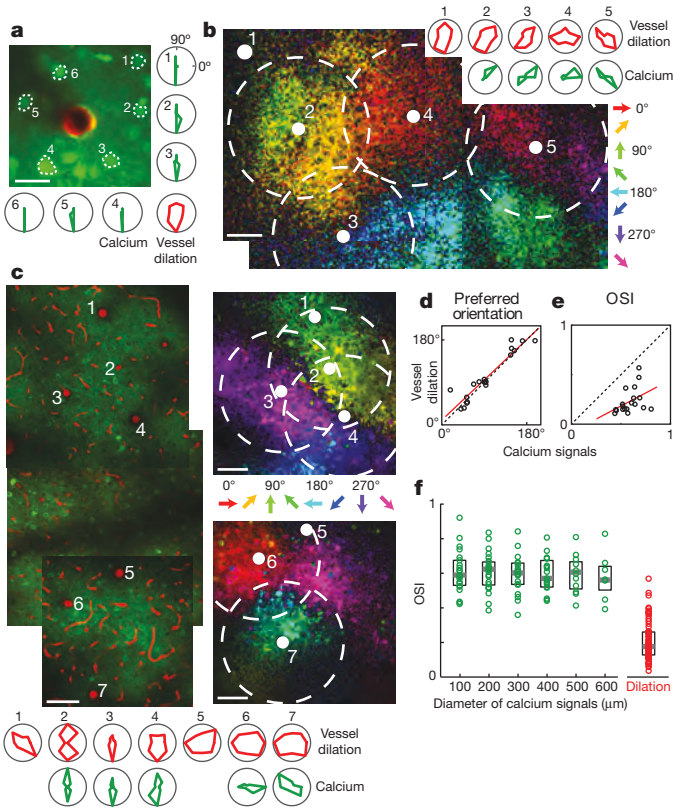

Figure 2 | Stimulus selectivity of single vessels and of spiking activity in the surrounding tissue. a, *In vivo* anatomical image of a small region of layer 2/3 cat visual cortex labelled with OGB-1 AM (green) and an arteriole labelled with Alexa 633 (red). Polar plots show the sensory evoked calcium responses from six neurons and the dilation of the arteriole. **b**, Pixel-based direction map and polar plots of responses from another cat labelled with OGB-1 AM and Alexa 633. The pixels are colour-coded by their preferred stimulus, with the brightness indicating the response strength. Red polar plots show the dilation responses of the five vessels indicated by solid white circles on the direction map. Green polar plots show the calcium responses pooled in 400-μm-diameter windows around four of these vessels (dashed circles). No calcium responses are shown for the region around vessel number 1 because this vessel was near the edge of the imaging field. **c**, Direction map and polar plots of responses from cat visual cortex labelled with GCaMP6s and blood vessels labelled with Texas Red Dextran. Left, tiled *in vivo* anatomical images of a large region of layer 2/3 where the positions of seven penetrating arterioles are numbered. Right, pixel-based direction maps of neural responses. The polar plots at the bottom show the vessel dilation responses (red) and the calcium responses (pooled over 400-μm-diameter regions) around five of these vessels (green). **d**, Correlation between the preferred orientation of the vessel dilation and the preferred orientation of calcium responses in 400-μm-diameter windows around each vessel ($R = 0.94$; $P < 10^{-8}$; $n = 19$ windows in 8 cats; regression line shown in red). **e**, No significant correlation between calcium and vessel OSI ($R = 0.41$; $P = 0.08$). **f**, Distribution of OSI for calcium responses across tissue regions of different window sizes ($n = 11$ cats) and for the population of dilation responses ($n = 18$ cats). Solid bars are medians and boxes indicate the interquartile range. For all window sizes, calcium responses were more selective than the vessel dilation ($P < 0.0001$, Mann–Whitney test). Pixel maps shown are averages of five to six trials. Scale bars, 25 μm (**a**) and 100 μm (**b**, **c**).

there was no correlation between the direction selectivity of a particular vessel and the glutamate signals in the surrounding tissue (Extended Data Fig. 3b; $R = 0.20$; $n = 37$ pairs; $P = 0.23$).

While vessel dilation responses over the population of parenchymal arterioles did not match neural orientation selectivity, we tested the possibility that the smallest vessels would show similar selectivity to neural responses. Larger penetrating arterioles (with baseline diameter >15 μm) may perfuse larger regions of tissue than small penetrating arterioles and their finer branches. Therefore, these smaller vessels (typically 8–15-μm baseline diameter) may be sensitive to vasodilators from smaller regions of neural tissue and thus have sharper orientation tuning. Indeed we found that OSI was inversely correlated with baseline vessel diameter in cat layer 2/3 (Extended Data Fig. 4a; $R = 0.37$, $P < 0.001$). We compared the dilation responses of these small vessels (baseline diameter ≤15 μm, mean = 11.8 μm) to those with baseline diameter >15 μm (based on consistency of Alexa 633 labelling[12]; see Methods). We found that the small vessels were slightly more tuned (OSI mean ± s.e.m. = 0.24 ± 0.02; $n = 35$) than the larger ones (OSI mean ± s.e.m. = 0.18 ± 0.01; $n = 44$; $P < 0.05$; Extended Data Fig. 4a, b). Importantly, however, the OSI of these small vessels was still lower than synaptic and spiking activity over the full range of window sizes ($P < 0.005$; see Extended Data Fig. 4b, c).

Capillaries are the smallest vessels in the neocortex and therefore may be even more tuned for stimulus orientation than small arterioles. However, whether capillaries have the capacity to dilate *in vivo* to sensory stimuli is controversial[13,14,18,19]. This is probably due to inconsistent criteria for defining capillaries and distinguishing them from pre-capillary arterioles as well as to the difficulty of detecting dilation in very small vessels even with two-photon microscopy resolution[13,14,18,19]. However, a small dilation in a capillary that is undetectable with two-photon microscopy would still lead to easily detectable changes in red blood cell (RBC) velocity. Because RBC size is slightly larger than the capillary lumen diameter, a very small dilation in a capillary could produce a dramatic reduction in the resistance to flow (see figure 2e in ref. 20). Therefore, we measured the stimulus-evoked changes in RBC velocity in a set of micro-vessels that would probably be classified as capillaries based on their high tortuosity and small diameter (4–7 μm; see Methods)[21,22]. We found that the orientation selectivity on the basis of blood velocity in these capillaries (OSI mean ± s.e.m. = 0.30 ± 0.04; $n = 15$ vessels) was no different from what was found for dilation of the ≤15-μm-diameter vessels ($P = 0.16$; Extended Data Fig. 4a, b). To determine if the tuning of capillaries was due to these vessels being in unusually broadly tuned windows of neural activity, we compared the OSI of neural activity around capillaries with what was found around parenchymal arterioles. The OSIs of 400-μm-diameter windows of spiking activity around capillaries (mean ± s.e.m. = 0.60 ± 0.03; $n = 13$) and around arterioles (mean ± s.e.m. = 0.59 ± 0.02; $n = 19$) were indistinguishable ($P = 0.94$, Mann–Whitney test). Thus, stimulus-evoked changes even in capillaries were still not as selective as the responses in adjacent neural tissue.

Our results suggest that blood flow increases in parenchymal vessels are partially driven by local neural activity (which would generate the match in orientation preference) and also by an additional global component arising from adjacent functional columns (which would induce the dilation to non-preferred orientations). One possibility is that this global component is due to the propagation of dilatory signals along vessel walls. Specifically, the lack of orientation tuning in surface arteries could result from the dilation of penetrating arterioles from many different orientation domains propagating back to a surface artery. Then the propagation of dilation along the surface artery and down into multiple penetrating arterioles could broaden the locally driven dilation signal, leading to dilation in adjacent regions of tissue that have no concomitant neural activity. Previous studies in rodents have demonstrated the propagation of dilation from the parenchyma up to the cortical surface[23] and along the surface over distances of at least 1 mm (refs 24–26) at rapid speeds[25], but these have not been linked to the stimulus selectivity of vessel or neural responses. Consistent with this propagation of dilation hypothesis, we found that in cat visual cortex parenchymal vessels dilate before the surface vessels and that the dilation to the preferred orientation came before the dilation to the stimulus that was oriented orthogonal to the preferred orientation, that is, at the null orientation (see Supplementary Information and Extended Data Fig. 5). Alternative

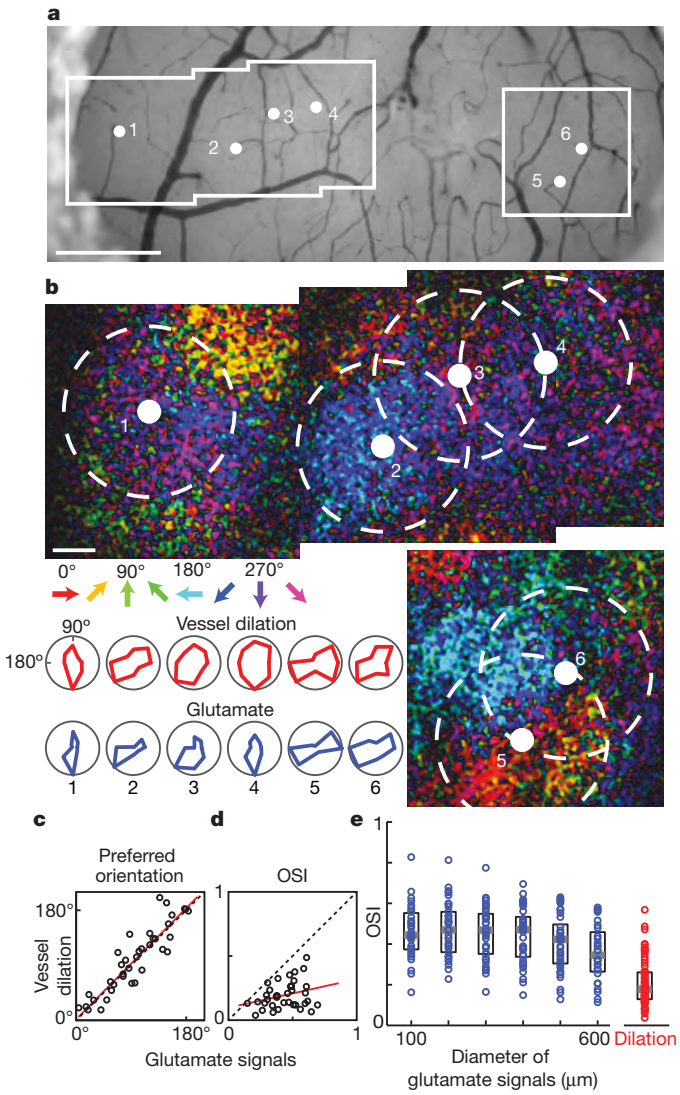

Figure 3 | Stimulus selectivity of single vessels and of excitatory synaptic activity in the surrounding tissue. a, Bright-field image of the surface of cat visual cortex showing the location of six penetrating arterioles and the regions targeted for two-photon imaging. **b**, Direction maps and polar plots of glutamate responses from cortical neurons labelled with iGluSnFR and dilation from blood vessels labelled with Texas Red Dextran. The positions of the arterioles and the 400-μm-diameter windows of pooled glutamate responses in cortical layer 2/3 are indicated by solid white and dashed circles, respectively. Red polar plots show the dilation responses and blue plots show the pooled glutamate activity in the windows around each arteriole. **c**, Correlation between the preferred orientation of the dilation responses and the preferred orientation of glutamate activity in 400-μm-diameter windows around each vessel for all cat data ($R = 0.90$, $P < 10^{-13}$; $n = 37$ windows in 5 cats). **d**, No significant correlation between glutamate and vessel OSI ($R = 0.28$, $P = 0.08$; linear regression line shown in red). **e**, Distribution of OSI for glutamate activity across windows of different sizes ($n = 5$ cats) and for the population of dilation responses ($n = 18$ cats). Solid bars are medians and boxes indicate the interquartile range. For all window sizes, the glutamate responses were more selective than vessel dilation ($P < 10^{-5}$, Mann–Whitney test). Pixel maps shown are averages of 8–10 trials. Scale bars, 500 μm (**a**) and 100 μm (**b**).

hypotheses on the origin of the selectivity of vessel dilation are discussed in Supplementary Information.

In conclusion, our results have a number of implications for the interpretation of haemodynamic signals in relation to neural activity. We provide direct single-vessel evidence for the untuned global signal in the pial vasculature that has been found in low-resolution haemodynamic imaging studies[27,28]. After subtracting the global signal, these earlier studies often suggested that the residual tuned vascular responses were of capillary origin[27,28]. We show that individual penetrating arteries also display stimulus-specific responses. Furthermore, the orientation selectivity of these parenchymal vessels is an order of magnitude higher than what is obtained with intrinsic signal optical imaging[29]. We also demonstrate that an organized functional map of neural responses is required for attaining tuned haemodynamic signals (see also ref. 30). Furthermore, by sampling responses over the full range of a stimulus parameter and by directly measuring synaptic and spiking activity along with single-vessel responses in precisely defined spatial regions of tissue, we overcome many of the technical limitations of earlier studies that examined neurovascular coupling. The difficulties inherent in correlating low-resolution vascular signals with electrophysiological metrics of neural activity and in interpreting glutamate pharmacology has led to controversy regarding the spatial scale over which synaptic versus spiking activity matches vascular signals (see Supplementary Information). Here we establish that the sensory stimulus that elicits the largest synaptic or spiking response also produces the largest haemodynamic signal. However, the complete selectivity profile of neither synaptic nor spiking activity in the local tissue around a vessel can be inferred from the tuning curves of haemodynamic signals. Thus, vascular signals are partially decoupled with local neural signals, over distances of at least 300 μm.

Online Content Methods, along with any additional Extended Data display items and Source Data, are available in the online version of the paper; references unique to these sections appear only in the online paper.

Received 14 July 2015; accepted 1 April 2016.
Published online 25 May 2016.

1. Raichle, M. E. & Mintun, M. A. Brain work and brain imaging. *Annu. Rev. Neurosci.* **29,** 449–476 (2006).
2. Grinvald, A., Lieke, E., Frostig, R. D., Gilbert, C. D. & Wiesel, T. N. Functional architecture of cortex revealed by optical imaging of intrinsic signals. *Nature* **324,** 361–364 (1986).
3. Heeger, D. J., Huk, A. C., Geisler, W. S. & Albrecht, D. G. Spikes versus BOLD: what does neuroimaging tell us about neuronal activity? *Nature Neurosci.* **3,** 631–633 (2000).
4. Logothetis, N. K., Pauls, J., Augath, M., Trinath, T. & Oeltermann, A. Neurophysiological investigation of the basis of the fMRI signal. *Nature* **412,** 150–157 (2001).
5. Sirotin, Y. B. & Das, A. Anticipatory haemodynamic signals in sensory cortex not predicted by local neuronal activity. *Nature* **457,** 475–479 (2009).
6. Maier, A. *et al.* Divergence of fMRI and neural signals in V1 during perceptual suppression in the awake monkey. *Nature Neurosci.* **11,** 1193–1200 (2008).
7. Wang, Z. & Roe, A. W. Columnar specificity of microvascular oxygenation and blood flow response in primary visual cortex: evaluation by local field potential and spiking activity. *J. Cereb. Blood Flow Metab.* **32,** 6–16 (2012).
8. Logothetis, N. K. What we can do and what we cannot do with fMRI. *Nature* **453,** 869–878 (2008).
9. Ekstrom, A. How and when the fMRI BOLD signal relates to underlying neural activity: the danger in dissociation. *Brain Res. Rev.* **62,** 233–244 (2010).
10. Ohki, K., Chung, S., Ch'ng, Y. H., Kara, P. & Reid, R. C. Functional imaging with cellular resolution reveals precise micro-architecture in visual cortex. *Nature* **433,** 597–603 (2005).
11. Kleinfeld, D. *et al.* A guide to delineate the logic of neurovascular signaling in the brain. *Front. Neuroenergetics* **3,** 1 (2011).
12. Shen, Z., Lu, Z., Chhatbar, P. Y., O'Herron, P. & Kara, P. An artery-specific fluorescent dye for studying neurovascular coupling. *Nature Methods* **9,** 273–276 (2012).
13. Drew, P. J., Shih, A. Y. & Kleinfeld, D. Fluctuating and sensory-induced vasodynamics in rodent cortex extend arteriole capacity. *Proc. Natl Acad. Sci. USA* **108,** 8473–8478 (2011).
14. Hillman, E. M. C. *et al.* Depth-resolved optical imaging and microscopy of vascular compartment dynamics during somatosensory stimulation. *Neuroimage* **35,** 89–104 (2007).
15. Shih, A. Y. *et al.* The smallest stroke: occlusion of one penetrating vessel leads to infarction and a cognitive deficit. *Nature Neurosci.* **16,** 55–63 (2013).
16. Attwell, D. *et al.* Glial and neuronal control of brain blood flow. *Nature* **468,** 232–243 (2010).
17. Howarth, C., Gleeson, P. & Attwell, D. Updated energy budgets for neural computation in the neocortex and cerebellum. *J. Cereb. Blood Flow Metab.* **32,** 1222–1232 (2012).
18. Hall, C. N. *et al.* Capillary pericytes regulate cerebral blood flow in health and disease. *Nature* **508,** 55–60 (2014).

19. Hill, R. A. *et al.* Regional blood flow in the normal and ischemic brain is controlled by arteriolar smooth muscle cell contractility and not by capillary pericytes. *Neuron* **87,** 95–110 (2015).
20. Blinder, P. *et al.* The cortical angiome: an interconnected vascular network with noncolumnar patterns of blood flow. *Nature Neurosci.* **16,** 889–897 (2013).
21. Kleinfeld, D., Mitra, P. P., Helmchen, F. & Denk, W. Fluctuations and stimulus-induced changes in blood flow observed in individual capillaries in layers 2 through 4 of rat neocortex. *Proc. Natl Acad. Sci. USA* **95,** 15741–15746 (1998).
22. Chhatbar, P. Y. & Kara, P. Improved blood velocity measurements with a hybrid image filtering and iterative Radon transform algorithm. *Front. Neurosci.* **7,** 106 (2013).
23. Tian, P. *et al.* Cortical depth-specific microvascular dilation underlies laminar differences in blood oxygenation level-dependent functional MRI signal. *Proc. Natl Acad. Sci. USA* **107,** 15246–15251 (2010).
24. Berwick, J. *et al.* Fine detail of neurovascular coupling revealed by spatiotemporal analysis of the hemodynamic response to single whisker stimulation in rat barrel cortex. *J. Neurophysiol.* **99,** 787–798 (2008).
25. Chen, B. R., Bouchard, M. B., McCaslin, A. F. H., Burgess, S. A. & Hillman, E. M. C. High-speed vascular dynamics of the hemodynamic response. *Neuroimage* **54,** 1021–1030 (2011).
26. Chen, B. R., Kozberg, M. G., Bouchard, M. B., Shaik, M. A. & Hillman, E. M. A critical role for the vascular endothelium in functional neurovascular coupling in the brain. *J. Am. Heart Assoc.* **3,** e000787 (2014).
27. Vanzetta, I., Slovin, H., Omer, D. B. & Grinvald, A. Columnar resolution of blood volume and oximetry functional maps in the behaving monkey; implications for fMRI. *Neuron* **42,** 843–854 (2004).
28. Fukuda, M. *et al.* Localization of activity-dependent changes in blood volume to submillimeter-scale functional domains in cat visual cortex. *Cereb. Cortex* **15,** 823–833 (2005).
29. Rao, S. C., Toth, L. J. & Sur, M. Optically imaged maps of orientation preference in primary visual cortex of cats and ferrets. *J. Comp. Neurol.* **387,** 358–370 (1997).
30. Li, Y., Van Hooser, S. D., Mazurek, M., White, L. E. & Fitzpatrick, D. Experience with moving visual stimuli drives the early development of cortical direction selectivity. *Nature* **456,** 952–956 (2008).

Supplementary Information is available in the online version of the paper.

Acknowledgements We thank A. Shih for comments on the manuscript. This work was supported by grants from the National Institutes of Health (NS088827), National Science Foundation (1539034), and Whitehall and Dana Foundations to P.K.

Author Contributions P.K. conceived and supervised the project. All authors collected data. P.O'H. and P.Y.C. analysed data. P.O'H., M.L. and P.K. wrote the paper. All authors commented on and approved the final manuscript.

Author Information Reprints and permissions information is available at www.nature.com/reprints. The authors declare no competing financial interests. Readers are welcome to comment on the online version of the paper. Correspondence and requests for materials should be addressed to P.K. (kara@musc.edu).

METHODS

Animals and surgery. All surgical and experimental procedures were approved by the Institutional Animal Care and Use Committee at Medical University of South Carolina. Cats ($n = 25$ of either sex; postnatal day 28 to >2.5 kg adult) were anaesthetized with isoflurane (1–2% during surgery, 0.5–1.0% during imaging) and paralyzed with a continuous infusion of vecuronium bromide (0.2 mg kg^{-1} h^{-1}, intravenously). Cats were artificially ventilated through a tracheal cannula, and the end tidal CO_2 was regulated at 3.5–4.5%. Heart rate, respiration rate, temperature and electroencephalogram were also monitored. Long Evans rats ($n = 10$ males, postnatal days 31–45) and C57BL/6J mice ($n = 1$ male, postnatal day 63) were initially anaesthetized with a bolus infusion of fentanyl citrate (0.04–0.06 mg kg^{-1}), midazolam (3.75–6.25 mg kg^{-1}), and dexmedetomidine (0.19–0.31 mg kg^{-1}). The one mouse was used for a control experiment to confirm that the iGluSnFR sensor was not being saturated during sensory stimulation (see later). During two-photon imaging, continuous intraperitoneal infusion with a lower concentration mixture (fentanyl citrate: 0.02–0.03 mg kg^{-1} h^{-1}; midazolam: 1.50–2.50 mg kg^{-1} h^{-1}; and dexmedetomidine: 0.10–0.25 mg kg^{-1} h^{-1}) was administered using a catheter connected to a syringe pump.

For all animals, craniotomies (2–3 mm square) were opened over the primary visual cortex (area 18), the dura was reflected, and the craniotomies were sealed with agarose (1.5–3% dissolved in artificial cerebrospinal fluid (ACSF)) and a glass coverslip. When the calcium indicator OGB-1 AM was used, before the placement of the coverglass, a pipette was inserted into the craniotomy and the dye was injected with air pressure puffs. The dye loading procedure has been described in detail[31].

In cats, we also used the genetically encoded indicators GCaMP6s[32] and iGluSnFR[33] to measure calcium and glutamate activity respectively. Two-to-four weeks before the imaging session, viral injections of AAV2/9.hSyn.GCaMP6s.WPRE.SV40 or AAV2/1.hSyn.iGluSnFR.WPRE.SV40 were performed under sterile surgery conditions. Cats were anaesthetized with 1–2% isoflurane and vital signs were monitored. One to three craniotomies were performed over the primary visual cortex (area 18) and small holes were made in the dura. Aliquots of virus (5 μl) were diluted in PBS and mannitol (5:9:6 ratio of virus:PBS:mannitol) to titres of ~10^{12} genomes ml^{-1} with 50–200 nl of Fast Green dye (Sigma) added to visualize the injection. Glass pipettes containing the virus solution were lowered 500–800 μm into the cortex and pressure puffs were administered over 15–20 min until approximately 1 μl had been injected. After 10 min, the pipettes were slowly retracted, the craniotomies were sealed with agarose (3% dissolved in ACSF), the scalp was sutured closed and the animals were recovered and returned to their housing. All animals were treated similarly and so randomization and blinding were not required. No statistical methods were used to predetermine sample size.

Two-photon imaging. For vascular imaging, three fluorescent dyes were used as we described previously[12]. Alexa 633 fluor hydrazide selectively labels artery walls, while Texas Red dextran (70 kDa) and fluorescein dextran (2,000 kDa) indiscriminately label the entire vascular lumen. Fluorescein dextran has similar excitation and emission properties as our neuronal labels OGB-1 AM, GCaMP6s, and iGluSnFR. Therefore, fluorescein dextran was not used for vessel dilation measurements in animals where neuronal imaging was performed because sufficient contrast between a vessel wall and background is more difficult to obtain when two green labels are used simultaneously. Fluorescein dextran was typically used for the measurement of RBC velocity and was only injected after the neural imaging was completed.

Fluorescence was monitored with a custom-built microscope (Prairie Technologies) coupled with a Mai Tai (Newport Spectra-Physics) mode-locked Ti:sapphire laser (810 nm or 920 nm) with DeepSee dispersion compensation. Excitation light was focused by a ×40 (NA 0.8, Olympus), ×20 (NA 1.0, Olympus) or ×16 (NA 0.8, Nikon) water immersion objective and beam expansion optics. Full frame imaging of neural activity and vessel dilation were typically obtained at approximately 0.8 Hz. All the blood velocity data and the dilation of a small number of vessels were measured with line scans rather than full frame imaging by using line acquisition rates between 0.4 and 4.2 kHz.

Visual stimulation and size of imaged region. Drifting square-wave grating stimuli were presented on a 17-inch LCD monitor. The gratings were presented at 100% contrast, 30 cd m^{-2} mean luminance, 1.5–2.0 Hz temporal frequency. As depicted in the various time courses (for example, Fig. 1) these stimuli were presented at eight directions of motion in 45° steps and each of these eight stimuli was interspersed with blank periods (equiluminant grey screen). Because vascular responses decay slowly, we used long blank periods (at least four times the stimulus duration) when measuring blood vessel responses. We also presented the eight visual stimuli in pseudo-random order. These steps ensured that a particular response would not be influenced by a residual response to the previous stimulus. The duration of the stimulation period, for example, 6 s, and the duration of the blank period, for example, 24 s, was always identical across all epochs in a stimulus sequence. Each of the eight stimuli was repeated at least three times and in the vast majority of the data, 5–10 trials were used. Unlike arteriole dilation, neural transients return to baseline nearly immediately upon extinguishing the visual stimulus[12,34] (see also Extended Data Figs 1 and 2). Therefore, for epochs of data collection involving only calcium or glutamate imaging, either sequential or pseudo-random sequences were used. While some neural and vascular data were collected simultaneously, our analyses benefited from collecting them sequentially for the following reasons. Neural data was typically collected in 600 × 600 μm square regions to allow the pooling of large regions of activity (see Figs 2b, c and 3b) and multiple 600 × 600 μm square regions were often imaged in a single craniotomy to obtain maps where many orientation and direction domains were represented (see Figs 2b, c, 3b and Extended Data Fig. 1). Higher pixel resolution was needed for resolving blood vessel dilation so we usually obtained the vessel responses immediately after the neural responses using higher optical zooms that were centred on the blood vessels of interest. Because of the optical zoom customization per imaged site and the differences in recovery of neural versus vascular responses to baseline, the selected duration of visual stimulation for a particular experiment ranged from 2 to 8 s and the duration of blank periods ranged from 6 to 35 s.

Data-analysis overview. Images were analysed in Matlab (Mathworks) and ImageJ (National Institutes of Health). Data with movements of several μm in XY or Z were excluded. Data with small drift movements were realigned by maximizing the correlation between frames.

Quantifying vessel dilation. We analysed dilation responses only in surface arteries and penetrating arterioles because veins and capillaries do not typically dilate to sensory stimuli less than 10 s in duration[12–14]. When veins dilate in response to very long duration sensory stimuli, these responses are relatively weak and extremely slow, unlike the rapid and large responses of arteries and arterioles[13]. Surface arteries and penetrating arterioles are distinguished from veins using Alexa 633 as an artery-specific dye, by their orange versus purplish hue under bright-field illumination, and by the tone of the vessel walls and the speed and direction of blood flow during two-photon imaging[12]. Distinguishing capillaries from pre-capillary arterioles has been inconsistent in the literature[13,14,18,19]. Here we categorize capillaries as vessels with 4–7 μm baseline diameter[21], high tortuosity and complete lack of Alexa-633 labelling[12]. Vessel diameter was determined in full-frame images by one of two methods. When the vessel had a circular profile (as was the case for most of the parenchymal arterioles), a region of interest was manually drawn around each vessel and a circle was fit to the pixels in the region that passed a luminance threshold (Extended Data Fig. 6). For vessels with an elongated profile (typical for pial surface vessels), a cross-section was taken through the vessel walls and the peaks in luminance (for the wall-labelling Alexa 633) or peaks in the pixel-by-pixel luminance difference along the line (for lumen labels) were used to compute the diameter[12] (see Extended Data Fig. 7). For the few instances where diameter was measured using line-scans, we averaged the data along the time axis over all the lines in an image (usually 1,000 lines) or obtained two data points per image by sequentially averaging half the lines in each image. Since each line was only 0.25–2.5 ms in duration, averaging across these lines still provided sufficient temporal resolution for capturing the onset, peak and recovery of sensory-evoked dilation. The diameter was computed from these line scans in the same way as for the cross-section (Extended Data Fig. 8). For all methods of dilation measurement, images were usually oversampled by interpolating between pixels from 2 to 20 times to allow the algorithm to compute diameter values with a spatial resolution that was finer than the pixel size in the raw data images. To compute the vascular response to each condition, a stimulus response window was defined. Because of the slow onset and offset of the vascular response, we could not simply assign the response period to correspond to the period when the stimulus was displayed on the monitor. Instead, for each vessel we selected the response period by examining the average response across all stimulus conditions and then selected the imaging frames that best approximated this response interval. Shifting this time window by adding or removing data points did not appreciably change the responses. The mean response across this time window was divided by the baseline level for each condition to get the percentage change in diameter. Responsive vessels were defined by ANOVA across baseline and eight directions over multiple trials ($P < 0.05$). The orientation selectivity index (OSI) was defined as:

$$\mathrm{OSI} = \mathrm{abs}\left(\frac{\sum_k r_k e^{i2\theta_k}}{\sum_k r_k}\right)$$

where θ_k is the orientation of each stimulus and r_k is the mean response across trials to that stimulus[35]. Note that OSI = 1 − circular variance. The preferred orientation was defined as: $\arctan(\Sigma r_k \cos(2\theta_k)/\Sigma r_k \sin(2\theta_k))$. The directionality index (DI) was computed as $1 - r_{\mathrm{null}}/r_{\mathrm{pref}}$, where r_{pref} is the response amplitude to the preferred stimulus and r_{null} is the response to the stimulus with the same orientation

drifting in the opposite direction. Computing the OSI based on flow rather than diameter by scaling the diameter values to the 4th power (Poiseuille's law) did not affect our results.

Measuring onset latency to dilation. To compare the latencies of pial arteries and parenchymal arterioles, we fit a linear regression line to the rising phase of the dilation (20–80% of the peak response) of each vessel. For parenchymal vessels, we used only the response to the preferred orientation because of potential latency differences between dilation to the preferred and other stimulus orientations (see later). For the pial vessels, we pooled the response to all stimulus conditions because these vessels are untuned to stimulus orientation. We used the time at which the regression line crossed the pre-stimulus baseline level as the onset latency[12]. This regression line metric on the average response is applicable when responses are large and relatively stable from trial to trial—as is the case for pial vessels to any stimulus orientation and for parenchymal vessels to the preferred stimulus orientation.

Since parenchymal vessels are orientation selective (Fig. 1b, d), responses to the null orientation are the weakest and, by definition, smallest in amplitude and more noisy from trial to trial. Thus, to compare the latency between the response to the preferred and null orientations in parenchymal vessels, we used a statistical test, the standardized mean difference (SMD, specifically Hedge's *g*; refs 36, 37), in which vessels are weighted by the trial-by-trial variance in latency values (see Extended Data Fig. 5a). We first smoothed each trial's time course with a three-frame running average. We then performed linear regression on the same interval as earlier (20–80% of the peak). We took the difference in the average onset latency across trials between the responses to preferred and null stimuli and standardized this difference by the pooled variability across the two conditions. The population summary SMD was obtained by using a random-effect model. This model weighs each vessel by the inverse variance of its SMD and factors in the heterogeneity present across the individual vessel data[37]. As a control for spurious effects, the preferred and null responses were assigned randomly for each trial and the analysis was repeated (Extended Data Fig. 5b).

Quantifying blood velocity. Velocity data was analysed as described previously[22]. Briefly, line scans were first pooled into blocks of 250, 500, or 1,000 lines. The angle of the RBC streaks in each image was used to determine the velocity of that block and a time course of velocity measurements was extracted. Baseline and stimulus windows were defined similarly to the dilation data and equivalent OSI and statistical analyses were performed.

Analysis of calcium and glutamate responses. Calcium and glutamate signals were analysed the same way. Raw images were first smoothed with a 4 μm Gaussian filter. The mean fluorescence of each pixel within a given 100–600-μm-diameter window around a vessel was computed for each blank and stimulus epoch. A *t*-test was performed on the difference in stimulus and baseline fluorescence for each condition in each trial and if the distribution was significantly higher than zero ($P < 0.05$), the pixel was included in the integration window. We also performed this analysis without excluding the unresponsive pixels and the responses were indistinguishable. In some data sets, part of the 100–600-μm-diameter analysis window fell outside of the image boundary and so there would be fewer pixels from those domains contributing to the overall response. Therefore, to avoid biasing the overall response of the integrated region, we divided the 100–600-μm-diameter analysis window into wedges before averaging the data over the full window. Each wedge was 1/16 of the circle and was further divided into sections of 50 μm radial length. Thus, a 100-μm-diameter window had 16 sections whereas a 400 μm-diameter window had 64. The pixels with significant responses within each section were averaged together to create a time course. The time course was then normalized by a sliding baseline of the mean fluorescence of each blank interval ($\Delta F/F$). Each time course was then weighted by the total number of pixels represented by its section, because sections farther from the vessel contain more pixels. Finally, the time courses of all the sections were averaged together to obtain the time course of the entire region. For inclusion in the population data set, responses from the 100–600-μm-diameter analysis windows had to pass the following criteria. First, each wedge had to have at least 30% of the imaged pixels passing the initial *t*-test to ensure that windows with wedges having no response and/or weak labelling would be removed. Second, at least 80% of the circular area of the window had to be within the image to ensure that a sizeable region of tissue whose orientation preference could dramatically affect the overall response was not being missed. In addition, at least 10% of each wedge had to be within the image to ensure that each wedge had some representation. For data that passed all these criteria, the responses to each condition were computed by averaging the imaging frames during stimulus presentation and across trials. Before the OSI was computed, if any conditions showed a negative response (below the baseline level), then the absolute value of the minimum response was added to all responses (to make the minimum equal zero). We have recently published a mechanistic rationale for applying such a correction in fluorescence imaging of neural responses—stimulus-evoked dilation of surface arteries can block fluorescence from the underlying tissue and make a very small response actually appear negative[12]. We also analysed the data without this correction and, in addition, when only including the first 1 s of the response (to avoid the slower surface artery interference[12]). Although there were small changes in the OSI values of individual windows, the overall results did not change in either case. The neural response amplitudes, OSI and DI were all computed using the same formulae as for the vessel data. Population distribution statistics on OSI and DI measurements used the Mann–Whitney test.

Additional control for calcium imaging. Spiking activity in the neuropil should also contribute to metabolic needs and hence neurovascular coupling. Therefore, when integrating the calcium signals in the tissue surrounding each artery, we included all pixels that passed a signal-to-noise criterion (see earlier) and not only those corresponding to cell bodies. However, the neuropil may include a mixture of calcium signals from synaptic events in dendritic spines and spiking in axons arriving from regions outside of the integration window we selected. Therefore, as a control, we compared the orientation selectivity in 400 μm-diameter windows with and without including the neuropil. Masks excluding the neuropil were generated in the same way as described earlier except that the pixels within each wedge were constrained to the cell bodies. Cell body masks were first created using an automated algorithm that applied a series of morphological filters to identify the contours of cell bodies based on intensity, size and shape[10]. Cell outlines were visually inspected and errors were corrected manually. Then a *t*-test was performed on each pixel of these masks and the wedges were created in the same manner as before. Because of the sparse distribution of cell bodies, we did not enforce the 30% significantly responding imaged pixels criterion but all other criteria applied. The orientation selectivity with the two mask types was indistinguishable (Extended Data Fig. 9).

Control to show that visual stimulation was not saturating the iGluSnFR sensor. With visual stimulation, the glutamate signals peaked at $<10\%$ $\Delta F/F$. To determine if the iGluSnFR sensor responded linearly and responded over a greater range than that obtained with visual stimulation, we used iontophoresis to apply large doses of exogenous glutamate. We lowered a pipette containing 0.5 M glutamate into layer 2/3 of the visual cortex of a mouse that was labelled with iGluSnFR. We applied a range of currents (10, 20, 40, 60, 80 nA) and found that the fluorescence signals increased linearly ($R > 0.99$; $P < 0.0001$) and peaked at $\sim$60% $\Delta F/F$ (data not shown). Thus, our *in vivo* imaging with iGluSnFR (for example, Extended Data Fig. 10) is probably revealing the true spatial profile of glutamate direction maps (Fig. 3) and orientation maps (Extended Data Fig. 1).

31. O'Herron, P. *et al.* Targeted labeling of neurons in a specific functional micro-domain of the neocortex by combining intrinsic signal and two-photon imaging. *J. Vis. Exp.* **70,** e50025 (2012).
32. Chen, T.-W. *et al.* Ultrasensitive fluorescent proteins for imaging neuronal activity. *Nature* **499,** 295–300 (2013).
33. Marvin, J. S. *et al.* An optimized fluorescent probe for visualizing glutamate neurotransmission. *Nature Methods* **10,** 162–170 (2013).
34. Kara, P. & Boyd, J. D. A micro-architecture for binocular disparity and ocular dominance in visual cortex. *Nature* **458,** 627–631 (2009).
35. Ringach, D. L., Shapley, R. M. & Hawken, M. J. Orientation selectivity in macaque V1: diversity and laminar dependence. *J. Neurosci.* **22,** 5639–5651 (2002).
36. Hedges, L. V. & Olkin, I. *Statistical Method for Meta-analysis* (Academic, 2014).
37. Chhatbar, P. Y. *et al.* Transcranial direct current stimulation post-stroke upper extremity motor recovery studies exhibit a dose-response relationship. *Brain Stimul.* **9,** 16–26 (2016).

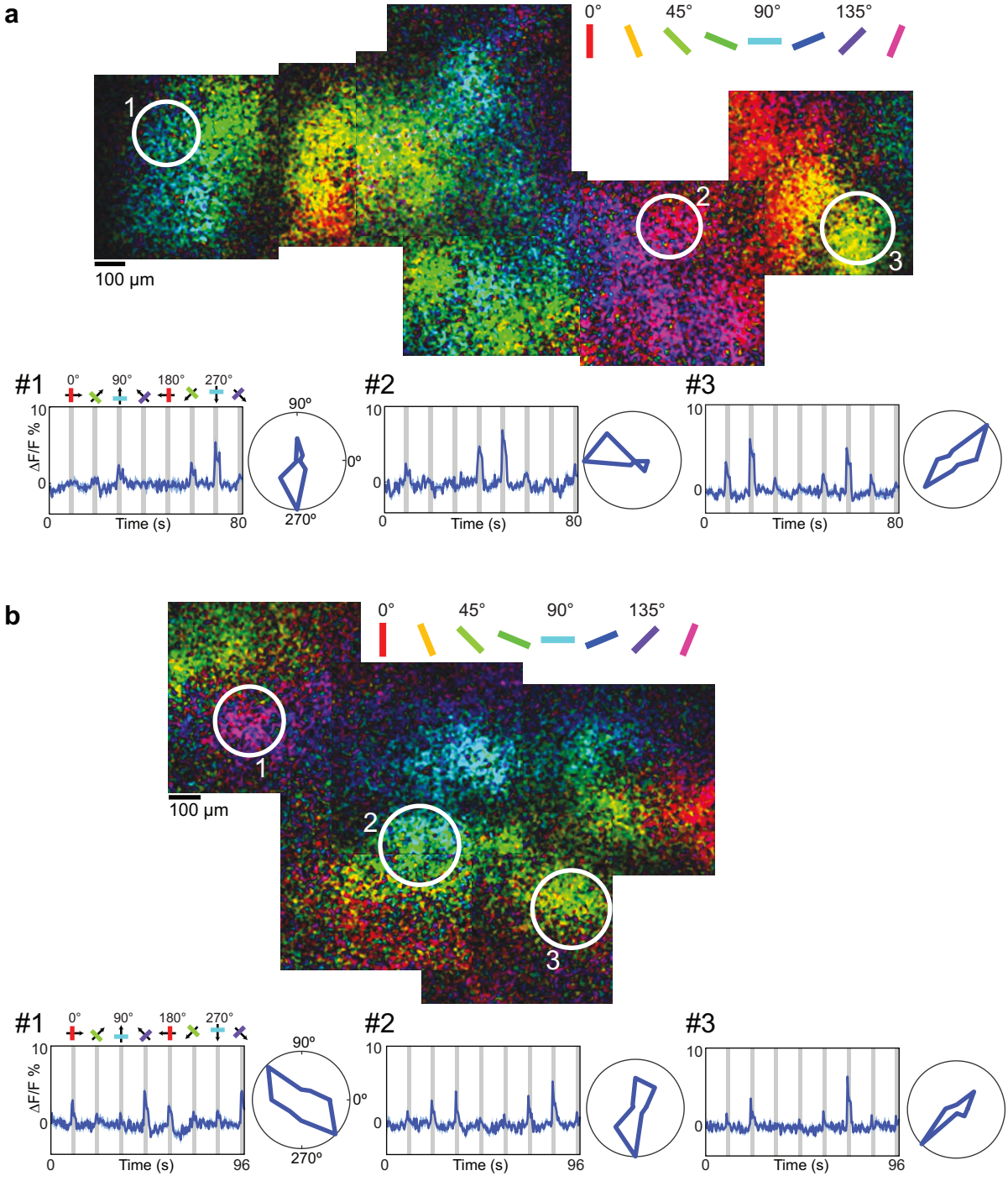

Extended Data Figure 1 | Glutamate release is organized into orientation maps. a, Region of cat visual cortex labelled with iGluSnFR. Pixels are colour-coded by preferred orientation with the brightness indicating the response strength. Time courses and polar plots (averages of four trials) are shown for three regions of tissue with different orientation preferences. **b**, Orientation maps of iGluSnFR responses from a different cat. Time courses and polar plots are averages of ten trials.

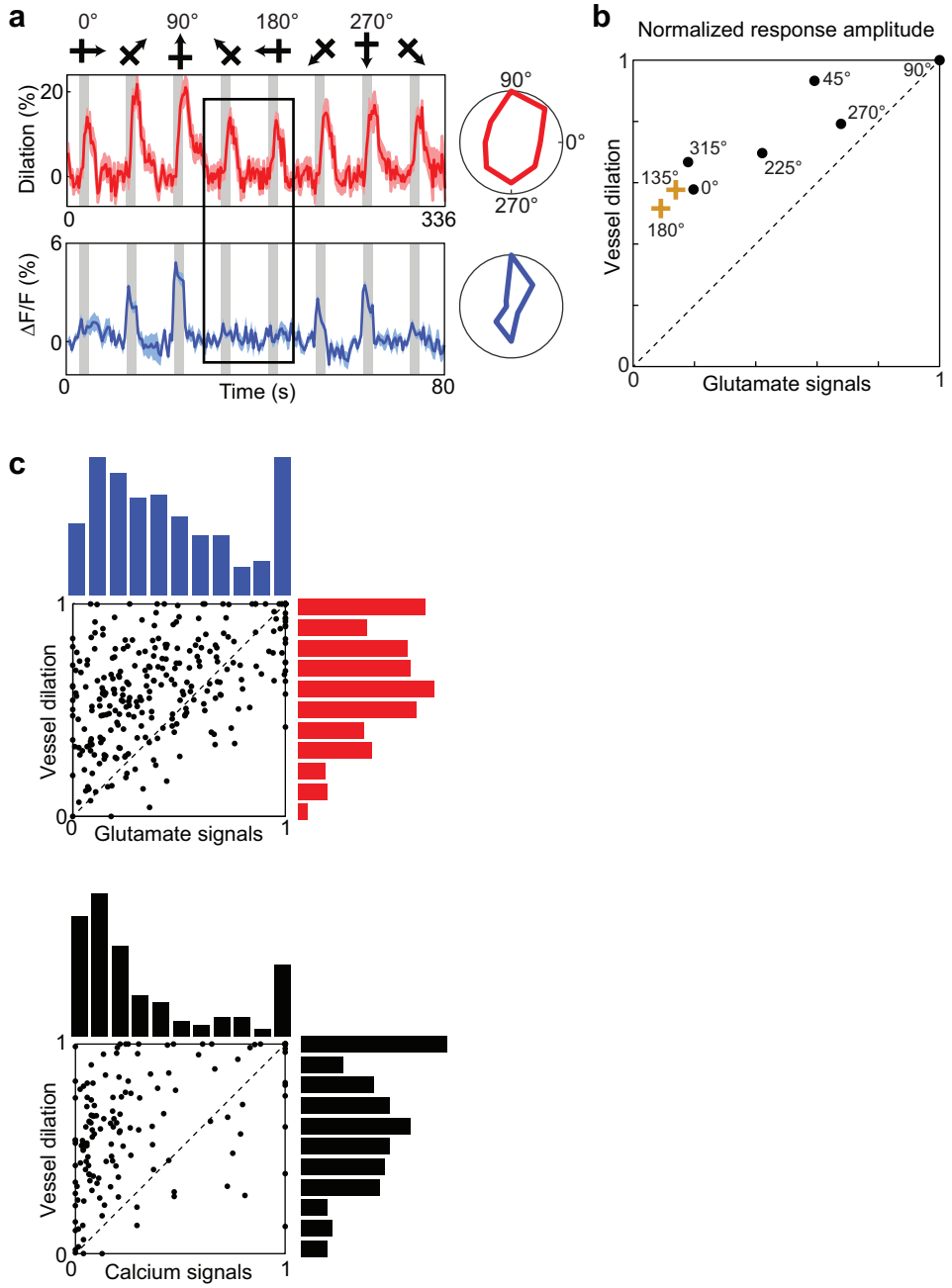

Extended Data Figure 2 | Arteriole dilation in the absence of glutamate signalling or local spiking. a, Time courses and polar plots of arteriole dilation (red) and the release of glutamate in a 400-μm-diameter window surrounding an arteriole (blue). Averages of eight trials are shown for vessel dilation and ten trials for glutamate responses. In time courses, error bands represent s.e.m. and grey bars represent the periods of visual stimulation. The responses to the 135° and 180° stimuli (outlined by the black box over the time courses) are large for the vessel dilation but virtually non-existent for the glutamate activity. **b**, Quantifying the relative amplitude of the vessel and neural responses to each of the eight stimulus directions for the single cat experiment shown in **a**. Each data point in the scatterplot represents the average response of the vessel and of the neural tissue surrounding it to a single direction of visual stimulation, normalized by the response to the best direction. **c**, Quantifying the relative amplitude of vessel and neural responses across all cat experiments. Top panel shows glutamate versus dilation data ($n = 37$ windows and vessels in 5 cats) and the bottom panel shows calcium versus dilation responses ($n = 19$ windows and vessels in 8 cats). Each data point in the scatterplot is as described in **b**. The histograms at the top and right show the distributions of neural and dilation responses, respectively. In both population scatterplots, there are many data points in the top left quadrant, indicating stimuli that drove robust dilation responses but minimal glutamate or calcium responses. All data are from cat visual cortex layer 2/3.

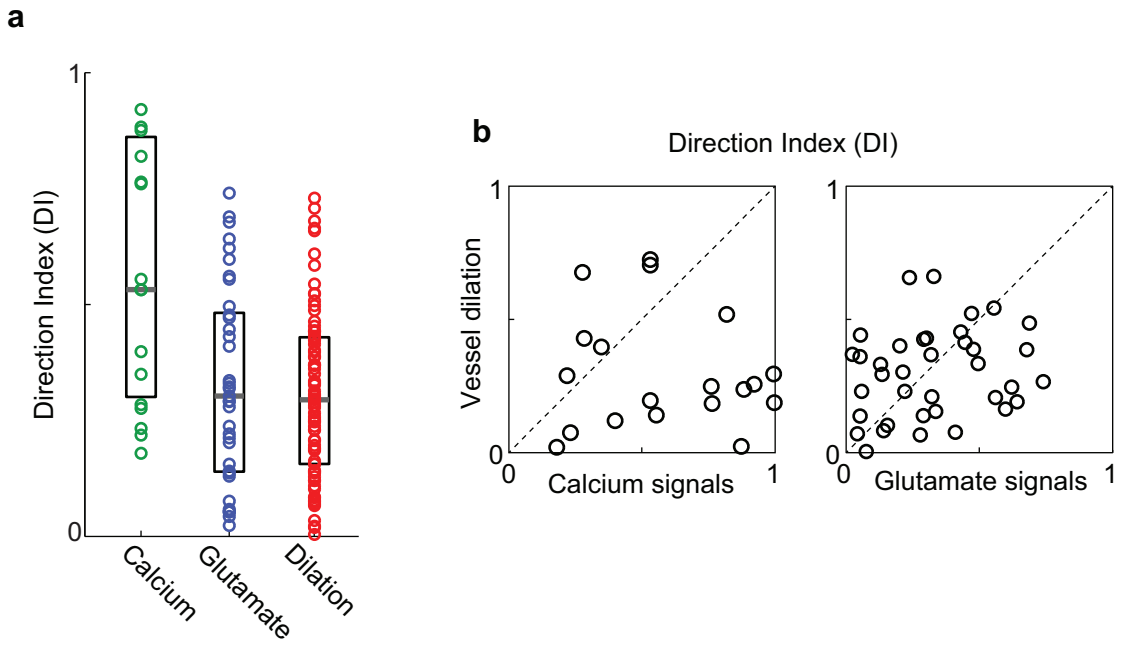

Extended Data Figure 3 | Direction selectivity of parenchymal vessels and of local spiking and synaptic activity. a, Population distributions of the direction index of calcium (green, $n = 19$ windows in 8 cats), glutamate (blue, $n = 37$ windows in 5 cats) and vessel dilation (red, $n = 79$ vessels in 18 cats) responses. All data were obtained from cat visual cortex and neural responses were pooled over 400-μm-diameter windows. The DI of spiking activity was greater than the DI of synaptic responses ($P < 0.01$, Mann–Whitney test) and the DI of vessel dilation ($P < 0.0005$, Mann–Whitney test). The DI of synaptic activity was not different from the DI of vessel dilation ($P = 0.70$, Mann–Whitney test). Solid bars are medians and boxes show the interquartile range. **b**, For each vessel that had a corresponding 400-μm-diameter window of calcium or glutamate activity, the vessel direction index is plotted against the corresponding neural direction index. There was no significant correlation for calcium ($R = 0.2$, $P = 0.43$, $n = 19$ pairs) or glutamate ($R = 0.2$, $P = 0.23$, $n = 37$ pairs).

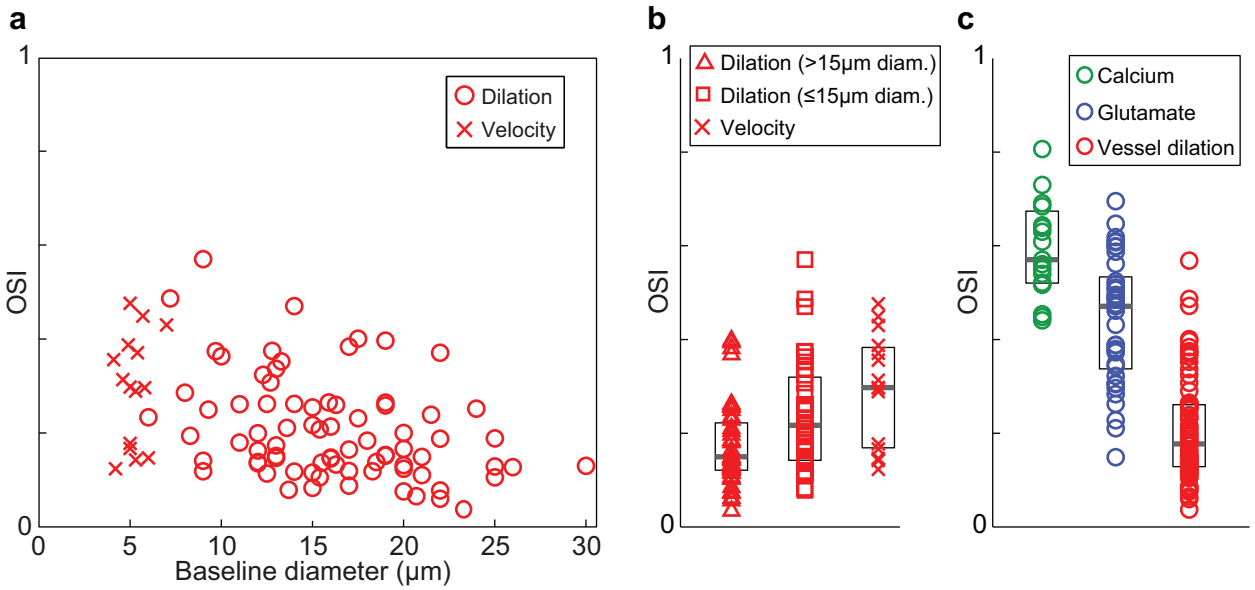

Extended Data Figure 4 | Dilation and velocity responses in parenchymal blood vessels with different baseline diameters. a, The diameter of all vessels and their OSI values from cat visual cortex layer 2/3. For arterioles, OSI was determined based on dilation ($n = 79$ vessels in 18 cats) whereas for capillaries, OSI was calculated from blood velocity measurements ($n = 15$ vessels in 7 cats). **b**, The distribution of OSI for the three subgroups of layer 2/3 vessels analysed in our study (>15 μm, $n = 44$ vessels in 15 cats; ≤15 μm, $n = 35$ vessels in 14 cats; capillaries, $n = 15$ vessels in 7 cats). The OSI of the ≤15 μm vessels was greater than the OSI of the >15 μm vessels ($P < 0.05$, Mann–Whitney test). The OSI of the ≤15 μm vessels was not different from the OSI of the capillaries ($P = 0.16$, Mann–Whitney test). Solid bars are medians and boxes indicate the interquartile range. **c**, The OSI distribution of dilating vessels and 400 μm-diameter windows of calcium and glutamate responses.

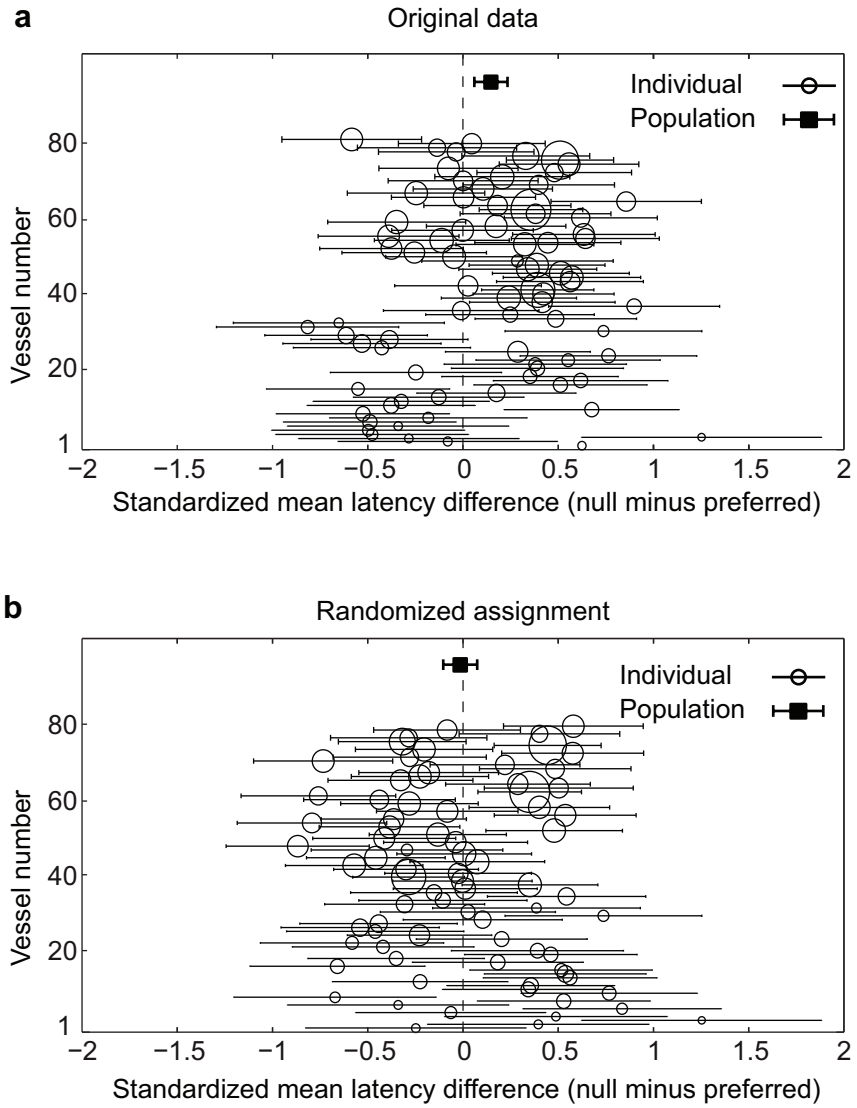

Extended Data Figure 5 | Onset latency of dilation in parenchymal vessels. a, Vessel-by-vessel comparison of the onset latency difference between the response to preferred and orthogonal (null) stimulus orientations. Each whisker diagram represents a single vessel with the circle position indicating the standardized mean difference (SMD; calculated as Hedge's *g*) in latency. The whisker length represents the 95% confidence interval (CI) of the SMD. The size of the circle represents the weight given to the vessel when calculating the population summary SMD. The population summary SMD is shown by the solid square with the error bands giving the 95% CI. The population average shows that parenchymal vessels responded significantly faster for the preferred than the null stimulus orientation. **b**, As a control, the analysis shown in **a** was repeated after randomizing the assignment of preferred and null on individual trials for each vessel. All data are from cat visual cortex layer 2/3 ($n = 79$ vessels in 18 cats).

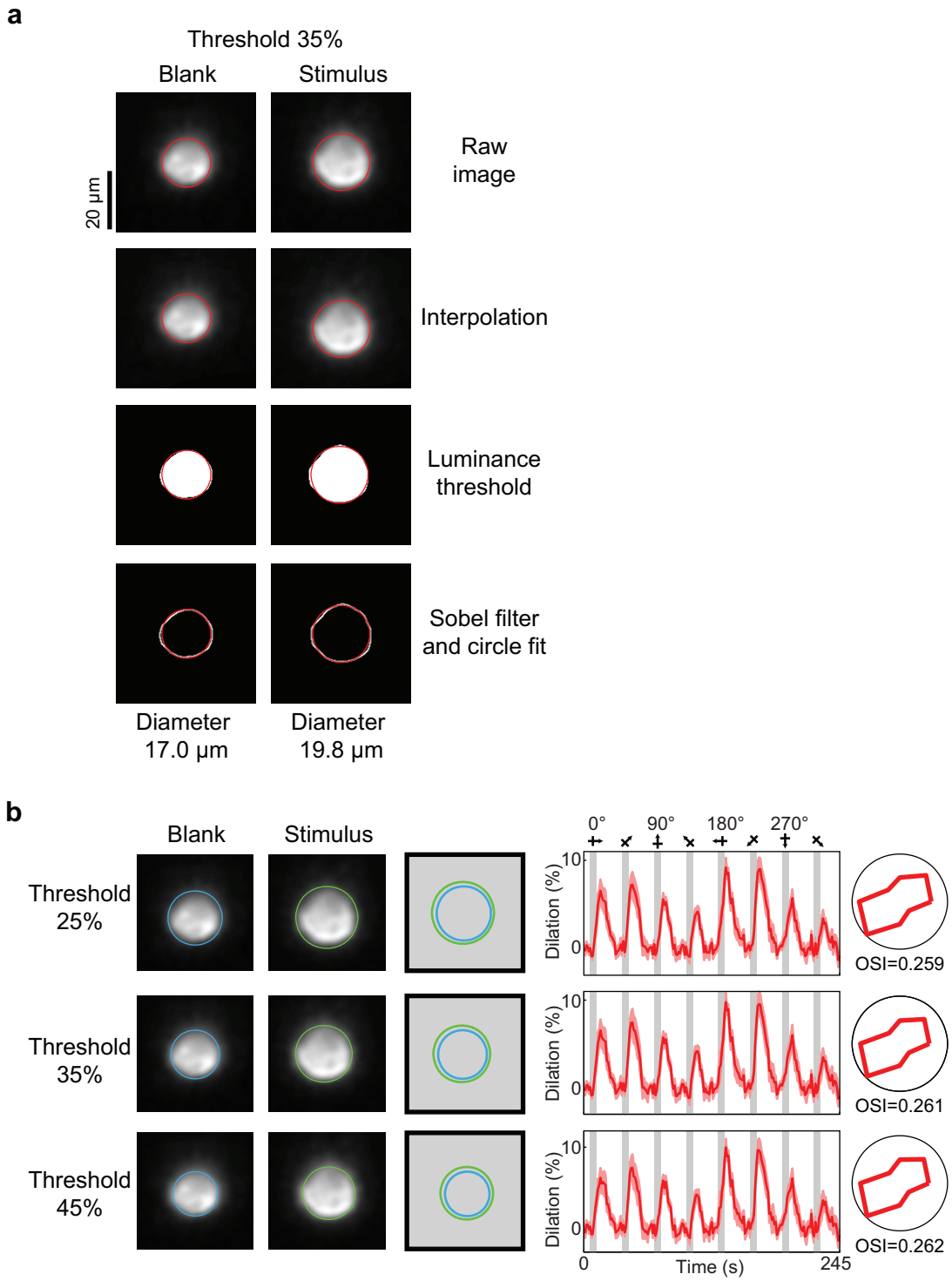

Extended Data Figure 6 | Dilation measurements with circle fitting. **a**, The steps of the circle fitting algorithm are illustrated for a blank and a stimulus frame corresponding to the penetrating arteriole shown in the bottom panel of Fig. 1b. The raw image data (first panel) is oversampled by linear interpolation between pixels (second panel). Then a luminance threshold (a fraction of the gradient between the brightest and darkest pixel of the image) is applied (third panel). Finally, a two-dimensional sobel filter is applied to the thresholded pixels to detect the edge of the vessel (fourth panel). The circle fit is only applied to the pixels in the fourth panel but it is overlaid on all the panels for illustration purposes. **b**, As the threshold is increased, fewer pixels pass the threshold and therefore the baseline diameter changes. However, the percentage change in diameter across baseline and stimulus presentations (the response amplitude) and the response selectivity remain the same. Note that for vessel geometries needing an elliptical fit rather than a circular fit (see Extended Data Fig. 8c and Methods), the shorter axis of the fitted ellipse was used to estimate the vessel diameter.

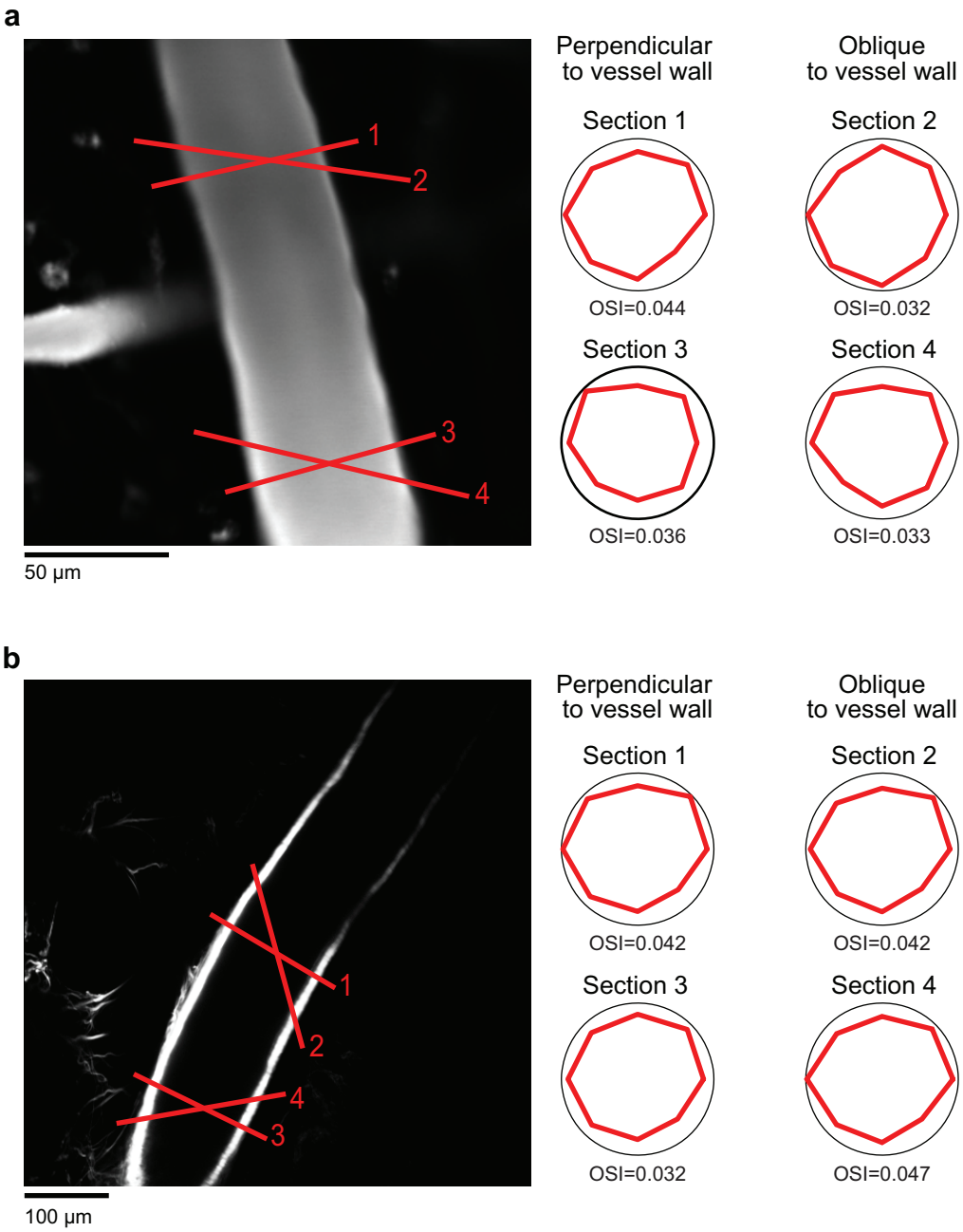

Extended Data Figure 7 | Dilation measurements using the cross-section algorithm do not depend on the precise location and angle of the selected cross-section. a, Example cat pial artery (from Fig. 1c) labelled with Texas Red Dextran. **b**, Another pial artery from a different cat labelled with the artery-specific dye Alexa 633. Both arteries show similar tuning for cross-sections drawn >100 µm apart and also drawn perpendicular and obliquely relative to the vessel walls.

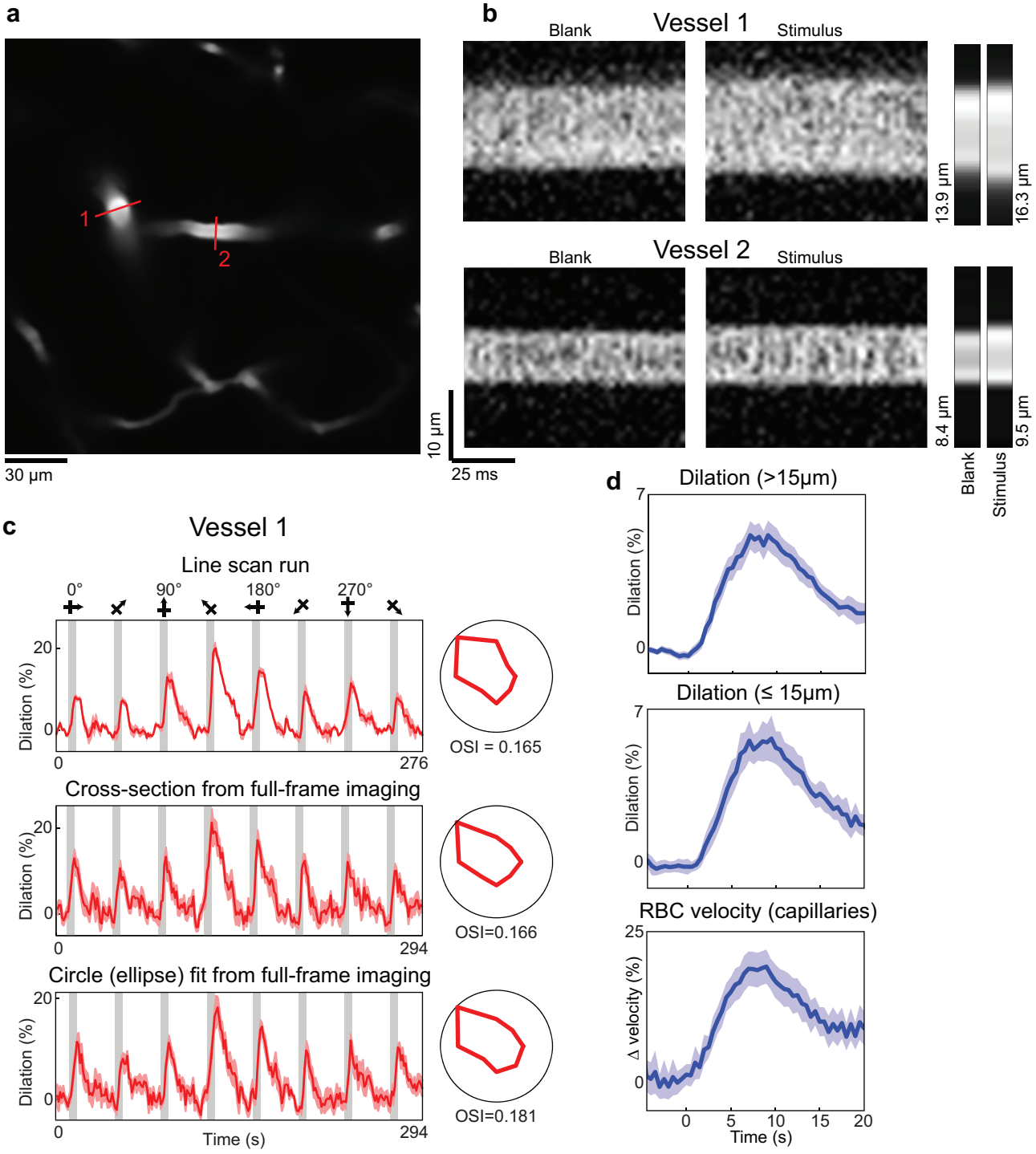

Extended Data Figure 8 | Dilation measurements in small arterioles and comparison of dilation measurement techniques. a, A penetrating artery (#1, the responses of which are shown in the top panel of Fig. 1b) and its daughter branch (#2) in cat layer 2/3 labelled with Texas Red Dextran. Red lines indicate the position of the laser scan path across the vessels for line-scan diameter measurements. **b**, Individual line-scans are stacked next to each other to create X-time (XT) images. The four large rectangular panels are XT images of a blank and stimulus frame for each of two vessels shown in **a**. The small panels to the right are the average across the image (~0.96 s) for each of the four frames. The computed diameter values are also shown. These images were oversampled by interpolating between pixels (by 5 times for vessel 1 and by 20 times for vessel 2) before the diameter was calculated. **c**, The time courses and polar plots of the responses for three different diameter measurements are shown for vessel 1—as a line-scan, a cross-section from a full-frame imaging run (seven trials), and the circle fit from the full-frame imaging run. In this particular example we used an ellipse rather than a circle because of the elongation of the vessel due to its diving obliquely to the imaging plane. **d**, Time courses of the vessel responses to preferred stimulus orientations for the three groups of vessels shown in Extended Data Fig. 4b. The responses for each vessel were aligned by stimulus onset and binned in 400-ms bins. The population average was then smoothed with a three-frame running average. Mean responses in dark colours and light bands indicate s.e.m. Note that the similar error bands and temporal profiles indicate that the smallest vessels had a similar quality of responses to the larger ones.

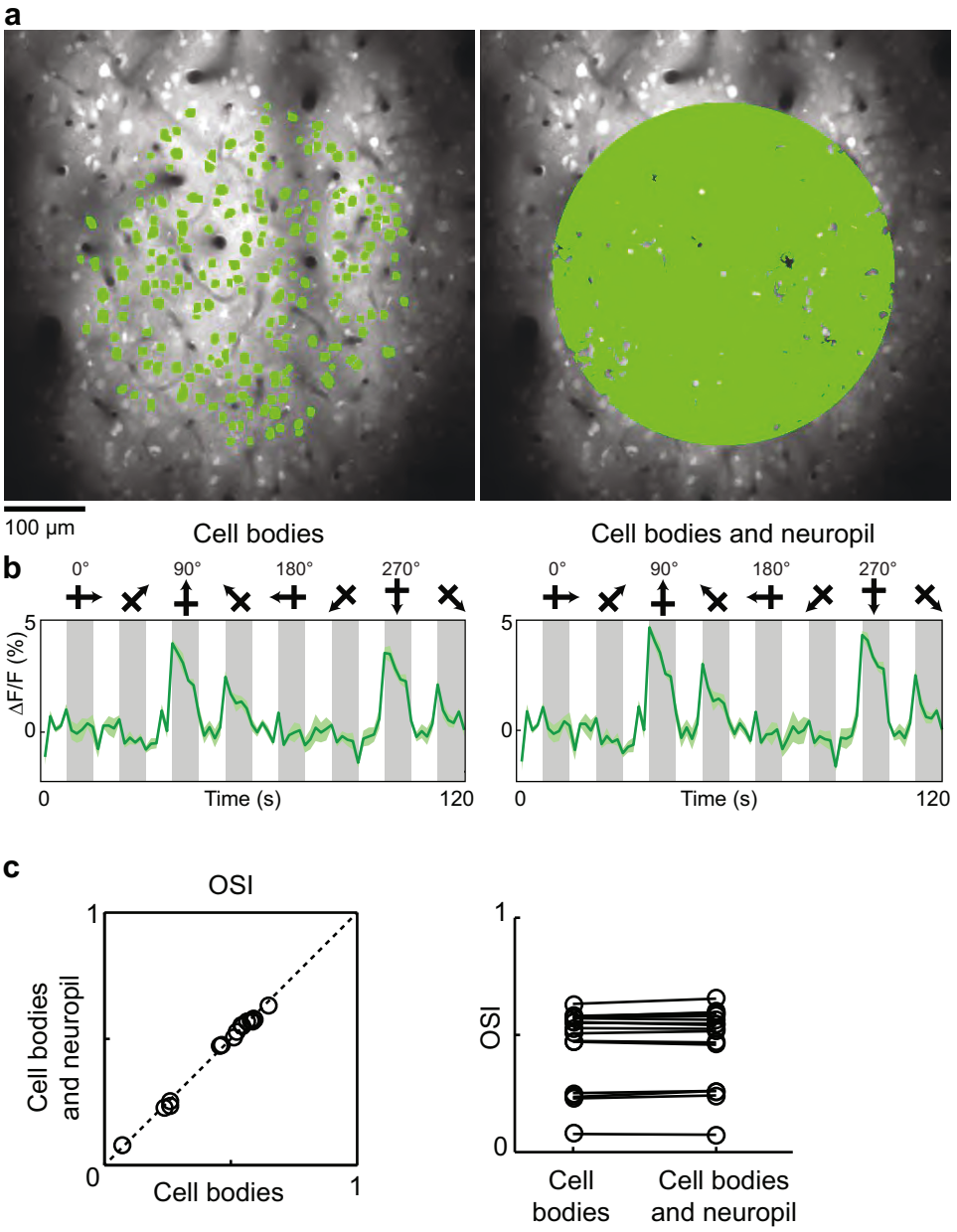

Extended Data Figure 9 | Comparison of orientation selectivity in regions of calcium responses with and without neuropil. a, *In vivo* anatomical image of cells labelled with OGB-1 AM in cat visual cortex and selection of two different masks for quantitative analysis of orientation selectivity. Left, a 400 µm-diameter mask comprising soma pixels only. Right, a 400 µm-diameter mask comprising all significantly responding pixels (see Methods). **b**, The time courses of calcium responses computed from the two masks. Time courses are averages of five trials, error bands represent s.e.m. and grey bars represent the periods of visual stimulation. **c**, For a population of 16 imaged regions (from 7 cats), the OSI was computed with the two masks and found to be indistinguishable (cell bodies only OSI mean ± s.e.m. = 0.46 ± 0.04; cell bodies and neuropil OSI mean ± s.e.m. = 0.47 ± 0.04; $P = 0.12$, paired t-test).

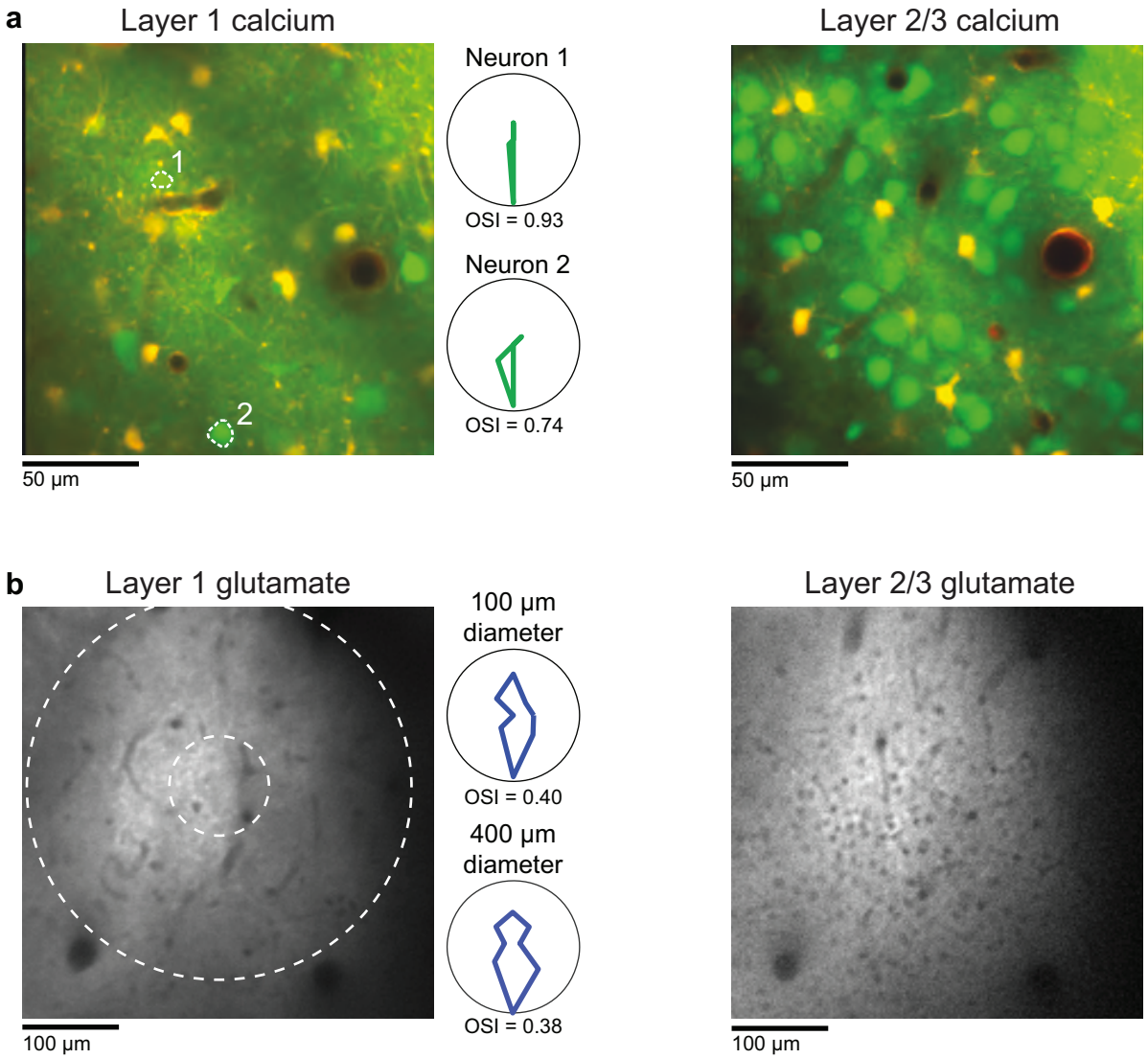

Extended Data Figure 10 | Orientation-selective responses in layer 1 neurons and synapses. a, Region of cat visual cortex labelled with OGB-1 AM (to measure spiking activity) and SR101 (to distinguish astrocytes). Note the much sparser density of neuronal cell bodies in layer 1 (left) compared with the higher density of cells deeper in layer 2/3 (right). The polar plots are the responses of the two layer 1 neurons labelled in the image. **b**, Region of cat visual cortex labelled with iGluSnFR (to measure synaptic activity). Again the density of cell bodies (the small black holes) in layer 1 (left) is much lower than in layer 2/3 (right). The polar plots are the responses of a 400-µm- and 100-µm-diameter window of layer 1 glutamate activity.

doi:10.1038/nature17965

1. Anatomical spacing of penetrating arterioles.

In rodent neocortex, the density of penetrating arterioles has been estimated to be anywhere between 4 and 13 per mm^2 (refs 15, 20, 38) and a similarly wide range has been reported in macaque neocortex as well[39,40]. In order to determine the spacing of arteries in our animals, we obtained large-scale z-stacks of the vasculature spanning 5.25 and 4.24 mm^2 per craniotomy in two cats. We used sequential *in vivo* two-photon imaging of 800 × 800 µm regions. These image stacks were then stitched together and the blood vessels in the large-scale stacks were traced using Neurolucida software (MBF Bioscience). We found that penetrating arteriole density was approximately 8–12 arterioles per mm^2, similar to what one report found in cats[41] (15.8 ± 1.2 arteries per mm^2). This density translates into an inter-arteriole spacing of approximately 300 µm and therefore a neural response window with 200 µm radius (400 µm diameter) around each vessel would provide adequate coverage, as we show in Figs. 2b,c and 3b. Our analysis also included other window sizes (100–600 µm diameter, see Figs. 2f and 3e).

2. Spatial scale of neurovascular coupling.

a. Techniques. Whether vascular signals correlate better with synaptic or spiking activity and the range of cortical tissue over which these signals are correlated are controversial[3-7,42-44]. Differences among past studies were in part probably due to the difficulty of measuring synaptic, spiking and haemodynamic signals over equivalent spatial scales. The spatial range over which neural activity may be pooled from extracellular electrophysiological recordings depends on a number of factors including the physical properties of the electrode as well as the type of neural activity being recorded. Well-isolated single-units (action potentials from different neurons) can typically be obtained from only a few cells per electrode and are heavily biased toward the largest and most active neurons near the electrode tip[45]. Multi-unit spiking activity can be obtained from up to a few thousand neurons over a range from tens to several hundred microns, and local field potentials (LFPs) pool low-frequency electrical activity over a range from a few hundred microns to several millimetres[8,46,47]. Furthermore, coarse-resolution haemodynamic imaging techniques, like fMRI, typically pool over even larger regions, making direct correlations between spiking, synaptic, and vascular activity difficult. An additional complication in these studies is that, although LFPs are used as a surrogate measurement of the synaptic activity in a region, it is still not known exactly how different features of neural activity

contribute to the LFP[46,48]. By imaging all of the neurons over a field of view along with individual vessels in the same region and by having a direct measure of synaptic activity we overcome these limitations.

b. Results. Typically, studies using low-resolution haemodynamic imaging and extracellular electrophysiology have found that haemodynamic signals spread well beyond the region of neural activation with point spread functions (PSFs) generally > 1 mm (refs 4, 49-51), although some studies have found conditions in which the spatial scales more closely match[24,52,53]. These studies correlate neural and vascular signals over spatial scales much larger in size (i.e., 500 μm to a couple of millimetres) than the regions we integrated over. Although we do not directly measure the complete spatial extent of neural and vascular signals, our finding of vascular responses in tissue where there is little to no concomitant neural activity indicates that vascular signals spread beyond the region of neural activity. However, despite the widespread range of vascular activity, haemodynamic signals have been used to discriminate functional columns in cortex with spacing < 1 mm including orientation columns[27,28,54-59]. Our results are consistent with these earlier studies because the preferred orientation of neighbouring arteries differs according to the preference of the neural tissue around each vessel. Thus, by simply looking at the preferred orientation of the dilation signal, orientation maps could be extracted from our data (see Figure 2b,c).

3. **Glutamate signalling driving vascular responses.**

We show that robust sensory-evoked vascular responses can often occur without a corresponding glutamate signal in the surrounding tissue, for example, Extended Data Fig. 2. Previous studies using pharmacological manipulations and low-resolution haemodynamic imaging in the neocortex have typically found that blocking post-synaptic glutamate receptors attenuates vascular responses[60-62], leading to the conclusion that local synaptic activity drives vascular responses (but see ref. 63). It is difficult to separate the effects of synaptic and spiking activity with a pharmacological approach because widespread application of glutamate receptor antagonists may also eliminate spiking activity across a large population of neurons. Note that because pharmacological agents are typically applied over very large areas of tissue, the remote activity generating the propagating dilation signal (as we propose) would be shut down. Therefore the localized uncoupling of neural and vascular activity that we observed may be

missed with a pharmacological approach. Indeed, an elegant two-photon imaging study in the olfactory bulb showed that a highly localized block of glutamate receptors did not affect blood flow but a widespread application of glutamate receptor antagonists reduced or eliminated it[64]. Note also that our finding of glutamate signals being less orientation selective than calcium signals is consistent with intracellular electrophysiological responses, for example, excitatory postsynaptic inputs show less orientation selectivity than neuronal spiking[65,66].

4. Origin of the selectivity of parenchymal vessel dilation to stimulus orientation.

The main findings of our paper regarding the parenchymal vasculature relate to the selectivity of responses in individual blood vessels along with the spatial regions of neural activity where selectivity may be matched. We assay two aspects of response selectivity in vessels and neural regions—the preferred stimulus and the degree of tuning to a complete set of oriented stimuli. The matching of neural and vessel responses to the best stimulus reaffirms the basic principle of functional hyperaemia—a blood flow increase is highest in the most active region of neural tissue. Finding a mismatch in the degree of orientation tuning between responses in vessels and the surrounding neural tissue was a complete surprise. This new information will be critical for the interpretation of data on response selectivity in all vascular-based imaging approaches such as intrinsic signal optical imaging, two-photon imaging and fMRI. Deciphering the exact origin of the less selective vascular signal could take many years to resolve and is beyond the scope of our study. However, below we present an analysis of our data that supports one possibility along with some alternatives that may be considered in future work.

a. Long-rage propagation of dilation from one cortical column into neighbouring columns. We propose that dilation signals in the absence of local neural activity are generated through long range propagation through the vascular wall[23,25,51]. This propagation has been estimated to travel along the vasculature at a speed of 2.4 mm/second[25]. Given that individual iso-orientation domains have widths in the range of several hundred microns (refs 2, 67), the dilation could propagate over a region of cortex that represents the entire span of orientations (a hypercolumn) within one second. Even though our imaging rates were <1 Hz for the majority of the data, we were able to detect differences in dilation onset latencies that were consistent with this hypothesis of a long-range propagated signal. According to our prediction, the local neural activity should first drive dilation in nearby arterioles which then propagates up to the surface[23].

Indeed we found that the onset latency was faster for parenchymal vessels (mean ± s.e.m. 1.63 ± 0.15 seconds; $n = 79$) than for pial vessels (2.12 ± 0.17 seconds; $n = 24$; $P < 0.05$, t-test; normal distributions confirmed with Lilliefors $P > 0.1$). Note that although we have a clear relative latency difference between the pial and the parenchymal vessels, because of the slow data acquisition rates used, the absolute numbers of the two groups may not reflect what would be obtained with faster sampling rates[12,23,25,68]. Our hypothesis also predicts that the broader vessel tuning relative to neural activity comes from the dilation signal initiated in vessels from different orientation columns into the vessel we are measuring. Thus, in parenchymal vessels, dilation to the preferred stimulus should appear earlier than dilation to the non-preferred stimulus. We computed the standardized mean difference (Hedge's g, see Methods) in dilation latency between the preferred and non-preferred orientations for each parenchymal vessel and found faster onset for the preferred orientation ($g = 0.15$; $P < 0.005$; Extended Data Fig. 5a). As a control, we randomized the assignment of the preferred and non-preferred orientations trial-by-trial across the population and found no latency difference ($g = 0.01$; $P = 0.78$; Extended Data Fig. 5b).

b. Long-range release of vasodilators. Another potential explanation for the vascular responses without corresponding neural activity is that blood vessels may be driven directly by neural activity from beyond the regions (300-µm-radius windows) we measured. However, it seems unlikely that vasodilating factors such as nitric oxide can diffuse over such long distances (> 300 µm) quickly enough to drive rapid stimulus-evoked dilation[69]. Additionally, because this distance substantially exceeds the inter-vessel spacing, it seems unlikely that a given penetrating arteriole would need to supply increased flow to such a large area of neural tissue and therefore should not be directly sensitive to distal neural activity. Long-range neuromodulatory inputs from extrastriate regions[6] and/or deep brain structures[5,70] have been proposed as the explanation of a large scale decoupling that has been found in awake behaving subjects. However, because our experiments were performed under anaesthesia, the fine-scale spatial decoupling we observed here (for example, Extended Data Fig. 2) is unlikely to originate from these neuromodulatory inputs.

c. Cortical laminar-dependent selectivity of neural responses. Compared to our primary measurements in cortical layer 2/3, it is possible that neural activity in other layers, for example, layer 4, is broader (less tuned for stimulus orientation) and represents the main driver of vascular

signals. These relatively weakly-tuned neural responses drive vessel dilation locally which might then propagate retrogradely over relatively short distances into layer 2/3, where we detect them (but see later). This short-range retrograde propagation is distinct from the long-range propagation into neighbouring columns that we propose in section 4a.

To examine the role of layer 1 activity in broadening the vascular response, we measured neuronal spiking and excitatory synaptic activity in layer 1 of cat visual cortex. Layer 1 in cat visual cortex has very few neuronal cell bodies but across three imaged regions in two cats, we obtained OSI values of spiking activity from 8 significantly responding neurons (Extended Data Fig. 10a) and found a mean value of 0.74. This layer 1 OSI of neuronal spiking activity was very similar to what we found in layer 2/3 neurons (see Fig. 2a). We also measured 400-μm-diameter windows of glutamate release in layer 1 of three cats and found a mean OSI of 0.38 (Extended Data Fig. 10b). This layer 1 OSI of synaptic activity was very similar to our layer 2/3 glutamate selectivity, but nearly twice as selective as the parenchymal blood vessel dilation (0.21). Thus layer 1 synaptic or spiking activity cannot be contributing the orientation selectivity of parenchymal dilation we measured in layer 2/3.

While existing techniques do not allow imaging the activity of the deeper layers (the layer 4 border is ~1 mm from the pial surface in cats), we think it is unlikely that neural activity in layers 4–6 contribute to the relatively broad orientation selectivity of haemodynamic responses in cat layer 2/3 blood vessels, for the following reasons:

Spiking. Almost all neurons in cat layer 4–6 have the same orientation selectivity as layer 2/3 neurons when measured with electrophysiological single-unit recording techniques[71-73].

Synaptic. Due to the uniformity of orientation selectivity of spiking activity across lamina[71-73] and the tendency of long-range connections to target similar orientation domains[74-76], the most likely cortical layer where synaptic activity could be untuned is where most of the thalamic inputs terminate in cat visual cortex, i.e., layer 4. Individual thalamic neurons and their axonal inputs are not orientation selective[77,78]. However, even though these thalamic inputs in cat visual cortex are strong with excitatory postsynaptic potentials (EPSPs) twice the size of unitary EPSPs evoked from other cortical neurons[79], these thalamic inputs only account for 6% of the glutamate synapses in layer 4 (ref. 80). Silencing all recurrent intracortical connections while sparing thalamic input activity eliminates most of the visually-evoked synaptic response[81] and the global haemodynamic response[82,83]. Finally, there are theoretical models[84,85] that support a

dominant role for intracortical connections in shaping the overall response and selectivity in cortical layer 4 neurons.

d. Inhibition. Another possible explanation for the mismatch between the selectivity in glutamate and vascular signals is that a specific subclass of neurons broadens the vascular response. In particular, certain types of inhibitory neurons have been shown to modulate arteriole diameter[86,87] and blood flow[60,88-90]. However, inhibitory neurons in layer 2/3 of the cat visual cortex are comparable to excitatory neurons in orientation selectivity[91]. Moreover, haemodynamic effects linked to inhibitory neurons are very slow, requiring up to dozens of seconds before arteriole diameter changes can be detected[86]. Ultimately, the development of fluorescent GABA sensors and the subsequent elucidation of spatial maps of GABAergic responses may resolve the specific role of GABA release in driving sensory-evoked haemodynamic responses. If combined with our iGluSnFR imaging of glutamate release, GABA imaging will provide more complete maps of synaptic transmission.

e. Astrocytes. Although astrocytes have been implicated in neurovascular coupling[16,92], we have not included them in our analysis. We examined the neural events that lead to vascular signals rather than the cellular and molecular mechanisms that transfer the neural signal to the vasculature. Thus whatever role astrocytes may play, it likely is downstream of the synaptic and spiking activity that trigger haemodynamic responses. However, astrocytes have been shown to have sharp orientation selectivity[93] and so they might be artificially increasing the selectivity of the calcium windows. We rule out this possibility for the following reasons. Firstly, astrocytes respond very slowly with onsets greater than 5 seconds[93], which is near the end of our typical neural response window. Secondly, although astrocytes are labelled with OGB, the GCaMP6 AAV serotype and promoter we used exclusively labels neurons and the selectivity of OGB labelled regions (OSI mean ± s.e.m. = 0.5898 ± 0.032, n = 12) was identical to that of the GCaMP6 labelled regions (0.5912 ± 0.034, n = 7; P = 0.95; Mann-Whitney test).

38 Nishimura, N., Schaffer, C. B., Friedman, B., Lyden, P. D. & Kleinfeld, D. Penetrating arterioles are a bottleneck in the perfusion of neocortex. *Proc. Natl. Acad. Sci. USA* **104**, 365-370 (2007).

39 Weber, B., Keller, A. L., Reichold, J. & Logothetis, N. K. The microvascular system of the striate and extrastriate visual cortex of the macaque. *Cereb Cortex* **18**, 2318-2330 (2008).

40 Adams, D. L., Piserchia, V., Economides, J. R. & Horton, J. C. Vascular Supply of the Cerebral Cortex is Specialized for Cell Layers but Not Columns. *Cereb Cortex* (2014).

41 McHedlishvili, G. & Kuridze, N. The modular organization of the pial arterial system in phylogeny. *J Cereb Blood Flow Metab* **4**, 391-396 (1984).

42 Rees, G., Friston, K. & Koch, C. A direct quantitative relationship between the functional properties of human and macaque V5. *Nat Neurosci* **3**, 716-723 (2000).

43 Lima, B., Cardoso, M. M., Sirotin, Y. B. & Das, A. Stimulus-related neuroimaging in task-engaged subjects is best predicted by concurrent spiking. *J. Neurosci.* **34**, 13878-13891 (2014).

44 Mathiesen, C., Caesar, K., Akgoren, N. & Lauritzen, M. Modification of activity-dependent increases of cerebral blood flow by excitatory synaptic activity and spikes in rat cerebellar cortex. *J Physiol* **512**, 555-566 (1998).

45 Olshausen, B. A. & Field, D. J. How close are we to understanding v1? *Neural Comput.* **17**, 1665-1699 (2005).

46 Berens, P., Keliris, G. A., Ecker, A. S., Logothetis, N. K. & Tolias, A. S. Feature selectivity of the gamma-band of the local field potential in primate primary visual cortex. *Front. Neurosci.* **2**, 199-207 (2008).

47 Xing, D., Yeh, C. I. & Shapley, R. M. Spatial spread of the local field potential and its laminar variation in visual cortex. *J. Neurosci.* **29**, 11540-11549 (2009).

48 Katzner, S. *et al.* Local origin of field potentials in visual cortex. *Neuron* **61**, 35-41 (2009).

49 Drake, C. T. & Iadecola, C. The role of neuronal signaling in controlling cerebral blood flow. *Brain and Language* **102**, 141-152 (2007).

50 Malonek, D. & Grinvald, A. Interactions between electrical activity and cortical microcirculation revealed by imaging spectroscopy: implications for functional brain mapping. *Science* **272**, 551-554 (1996).

51 Iadecola, C., Yang, G., Ebner, T. J. & Chen, G. Local and propagated vascular responses evoked by focal synaptic activity in cerebellar cortex. *J Neurophysiol* **78**, 651-659 (1997).

52 Vazquez, A. L., Fukuda, M., Crowley, J. C. & Kim, S. G. Neural and hemodynamic responses elicited by forelimb- and photo-stimulation in channelrhodopsin-2 mice: insights into the hemodynamic point spread function. *Cereb Cortex* **24**, 2908-2919 (2014).

53 Li, N., van Zijl, P., Thakor, N. & Pelled, G. Study of the spatial correlation between neuronal activity and BOLD fMRI responses evoked by sensory and channelrhodopsin-2 stimulation in the rat somatosensory cortex. *Journal of molecular neuroscience : MN* **53**, 553-561 (2014).

54 Bonhoeffer, T. & Grinvald, A. Iso-orientation domains in cat visual cortex are arranged in pinwheel-like patterns. *Nature* **353**, 429-431 (1991).

55 Fukuda, M., Moon, C. H., Wang, P. & Kim, S. G. Mapping iso-orientation columns by contrast agent-enhanced functional magnetic resonance imaging: reproducibility, specificity, and evaluation by optical imaging of intrinsic signal. *J Neurosci* **26**, 11821-11832 (2006).

56 Duong, T. Q., Kim, D. S., Ugurbil, K. & Kim, S. G. Localized cerebral blood flow response at submillimeter columnar resolution. *Proc Natl Acad Sci U S A* **98**, 10904-10909 (2001).

57 Sheth, S. A. *et al.* Columnar Specificity of Microvascular Oxygenation and Volume Responses: Implications for Functional Brain Mapping. *The Journal of Neuroscience* **24**, 634-641 (2004).

58 Moon, C. H., Fukuda, M. & Kim, S.-G. Spatiotemporal characteristics and vascular sources of neural-specific and -nonspecific fMRI signals at submillimeter columnar resolution. *NeuroImage* **64**, 91-103 (2013).

59 Yacoub, E., Harel, N. & Uğurbil, K. High-field fMRI unveils orientation columns in humans. *Proceedings of the National Academy of Sciences* **105**, 10607-10612 (2008).

60 Lecrux, C. *et al.* Pyramidal neurons are "neurogenic hubs" in the neurovascular coupling response to whisker stimulation. *J. Neurosci.* **31**, 9836-9847 (2011).

61 Nielsen, A. N. & Lauritzen, M. Coupling and uncoupling of activity-dependent increases of neuronal activity and blood flow in rat somatosensory cortex. *J Physiol* **533**, 773-785 (2001).

62 Lauritzen, M. Reading vascular changes in brain imaging: is dendritic calcium the key? *Nat Rev Neurosci* **6**, 77-85 (2005).

63 Scott, N. A. & Murphy, T. H. Hemodynamic responses evoked by neuronal stimulation via channelrhodopsin-2 can be independent of intracortical glutamatergic synaptic transmission. *PLoS One* **7**, e29859 (2012).

64 Chaigneau, E. *et al.* The relationship between blood flow and neuronal activity in the rodent olfactory bulb. *J. Neurosci.* **27**, 6452-6460 (2007).

65 Carandini, M. & Ferster, D. Membrane potential and firing rate in cat primary visual cortex. *J Neurosci* **20**, 470-484 (2000).

66 Marino, J. *et al.* Invariant computations in local cortical networks with balanced excitation and inhibition. *Nature Neuroscience* **8**, 194-201 (2005).

67 Ohki, K. *et al.* Highly ordered arrangement of single neurons in orientation pinwheels. *Nature* **442**, 925-928 (2006).

68 Nizar, K. *et al.* In vivo Stimulus-Induced Vasodilation Occurs without IP3 Receptor Activation and May Precede Astrocytic Calcium Increase. *The Journal of Neuroscience* **33**, 8411-8422 (2013).

69 Lancaster Jr, J. R. A Tutorial on the Diffusibility and Reactivity of Free Nitric Oxide. *Nitric Oxide* **1**, 18-30 (1997).

70 Tan, C. O. Anticipatory changes in regional cerebral hemodynamics: a new role for dopamine? *J Neurophysiol* **101**, 2738-2740 (2009).

71 Murphy, P. C. & Sillito, A. M. Continuity of orientation columns between superficial and deep laminae of the cat primary visual cortex. *J Physiol* **381**, 95-110 (1986).

72 Alonso, J. M. & Martinez, L. M. Functional connectivity between simple cells and complex cells in cat striate cortex. *Nat Neurosci* **1**, 395-403 (1998).

73 Shmuel, A. & Grinvald, A. Functional organization for direction of motion and its relationship to orientation maps in cat area 18. *J Neurosci* **16**, 6945-6964 (1996).

74 Gilbert, C. & Wiesel, T. Columnar specificity of intrinsic horizontal and corticocortical connections in cat visual cortex. *The Journal of Neuroscience* **9**, 2432-2442 (1989).

75 Bosking, W. H., Zhang, Y., Schofield, B. & Fitzpatrick, D. Orientation Selectivity and the Arrangement of Horizontal Connections in Tree Shrew Striate Cortex. *The Journal of Neuroscience* **17**, 2112-2127 (1997).

76 Malach, R., Amir, Y., Harel, M. & Grinvald, A. Relationship between intrinsic connections and functional architecture revealed by optical imaging and in vivo targeted

biocytin injections in primate striate cortex. *Proceedings of the National Academy of Sciences* **90**, 10469-10473 (1993).
77 Reid, R. C. & Alonso, J. M. Specificity of monosynaptic connections from thalamus to visual cortex. *Nature* **378**, 281-284 (1995).
78 Kara, P., Reinagel, P. & Reid, R. C. Low response variability in simultaneously recorded retinal, thalamic, and cortical neurons. *Neuron* **27**, 635-646 (2000).
79 Stratford, K. J., Tarczy-Hornoch, K., Martin, K. A., Bannister, N. J. & Jack, J. J. Excitatory synaptic inputs to spiny stellate cells in cat visual cortex. *Nature* **382**, 258-261 (1996).
80 Ahmed, B., Anderson, J. C., Douglas, R. J., Martin, K. A. & Nelson, J. C. Polyneuronal innervation of spiny stellate neurons in cat visual cortex. *J Comp Neurol* **341**, 39-49 (1994).
81 Ferster, D., Chung, S. & Wheat, H. Orientation selectivity of thalamic input to simple cells of cat visual cortex. *Nature* **380**, 249-252 (1996).
82 Radhakrishnan, H., Wu, W., Boas, D. & Franceschini, M. A. Study of neurovascular coupling by modulating neuronal activity with GABA. *Brain research* **1372**, 1-12 (2011).
83 Harris, S., Jones, M., Zheng, Y. & Berwick, J. Does neural input or processing play a greater role in the magnitude of neuroimaging signals? *Frontiers in Neuroenergetics* **2** (2010).
84 Douglas, R. J., Koch, C., Mahowald, M., Martin, K. A. & Suarez, H. H. Recurrent excitation in neocortical circuits. *Science* **269**, 981-985 (1995).
85 Somers, D. C., Nelson, S. B. & Sur, M. An emergent model of orientation selectivity in cat visual cortical simple cells. *J Neurosci* **15**, 5448-5465 (1995).
86 Cauli, B. *et al.* Cortical GABA interneurons in neurovascular coupling: relays for subcortical vasoactive pathways. *J. Neurosci.* **24**, 8940-8949 (2004).
87 Cauli, B. & Hamel, E. Revisiting the role of neurons in neurovascular coupling. *Frontiers in neuroenergetics* **2**, 9 (2010).
88 Shmuel, A., Augath, M., Oeltermann, A. & Logothetis, N. K. Negative functional MRI response correlates with decreases in neuronal activity in monkey visual area V1. *Nat. Neurosci.* **9**, 569-577 (2006).
89 Devor, A. *et al.* Suppressed neuronal activity and concurrent arteriolar vasoconstriction may explain negative blood oxygenation level-dependent signal. *J. Neurosci.* **27**, 4452-4459 (2007).
90 Anenberg, E., Chan, A. W., Xie, Y., LeDue, J. M. & Murphy, T. H. Optogenetic stimulation of GABA neurons can decrease local neuronal activity while increasing cortical blood flow. *J. Cereb. Blood Flow Metab.* (2015).
91 Keller, A. J. & Martin, K. A. C. Local Circuits for Contrast Normalization and Adaptation Investigated with Two-Photon Imaging in Cat Primary Visual Cortex. *J. Neurosci.* **35**, 10078-10087 (2015).
92 Petzold, G. C. & Murthy, V. N. Role of astrocytes in neurovascular coupling. *Neuron* **71**, 782-797 (2011).
93 Schummers, J., Yu, H. & Sur, M. Tuned responses of astrocytes and their influence on hemodynamic signals in the visual cortex. *Science* **320**, 1638-1643 (2008).